

Collinear Laser Spectroscopy on Exotic Isotopes of Rubidium and Gallium

Walaa Al Tamimi

Doctor of Philosophy

Department of Physics

McGill University

Montreal, Quebec

October 28, 2016

A thesis submitted in partial fulfilment of the requirements for the degree of Doctor
of Philosophy in the Faculty of Science

©Walaa Rehab Al Tamimi

DEDICATION

*dedicated to my little blessings, Mohanad, Jana, and Joann.
You have made me stronger, better and more fulfilled than I
could have ever imagined.*

ACKNOWLEDGEMENTS

This thesis was done as a part of the laser spectroscopy group collaboration at TRIUMF, without whom none of this could have been achieved. I am profoundly thankful to Dr. Fritz Buchinger for the opportunity afforded to me to pursue my PhD degree at McGill University, accompanied by a great scientific experience at TRIUMF. I am also thankful to Prof. John Crawford for his assistance from the first steps in the laser spectroscopy world and understanding hyperfine structure. Although it was difficult at times, I enjoyed every challenging project that was assigned to me during the past 4 years.

I am most grateful to have worked under the supervision of Dr. Matt Pearson whilst at TRIUMF, who has been a wonderful supervisor and one of the best team leaders I have ever worked with. He has taught me a lot about laser spectroscopy. I am more confident in my understanding of the physics and the techniques behind the theory. I can build a laser optics table from scratch now! Thank you Matt for everything.

I would like to thank the TRIUMF centre committee who had a great impact on my professional career as well as my personal development. The organised summer schools, the workshops, the seminars and the nuclear physics courses that were offered contributed significantly to my growth. I am blessed for meeting such a great group of women in nuclear physics whilst at TRIUMF. I would like to sincerely thank Dr. Ania Kwiatkowski for her time and thoughts, for her professional and emotional support, and for her valuable feedback on my thesis. A special thanks go to Dr. Monika Stachura and Dr. Sonia Bacca for the support they provided. I am

proud to be a member of the laser spectroscopy group at TRIUMF, to which I hope to contribute further in the future . I would like to thank Dr. Annika Voss , and Dr. Bradley Cheal for their valuable contributions during the experiments and the analysis of this work. I am also grateful to Dr. Tom Procter for all the help and the explanations during his work at TRIUMF. A special thanks to to my McGill, TRIUMF , and life colleague and friend , Allen Leary. A Non forgettable members who have been very creative and helpful during their stay with the group. I would like to thank Julien Refour for his contribution to the gallium experiment as well as practicing his French in translating my English abstract. Thanks to Joanna Huang for her help in polishing this thesis.

Back in Jordan, I would like to thank the University of Jordan for awarding me a scholarship to pursue my Ph. D. degree in experimental nuclear physics. I am thankful to prof. Mahmoud Jaghoub from the physics department at the university of Jordan for his follow ups and encouragement. I would like to like to thank Prof. Saed Dababneh, an inspirational pillar in the nuclear physics field in Jordan for his encouragement.

I am proudly thankful to my extensive network of familial support that has been there for me through thick and thin. In particular my father , my honor , to whom who had pass the idea of doing a master in physics. I would like to tell you I completed a master in physics, and now I am honored to give you a higher degree to be proud of. To my mother, thank you for your secret blessings and prayers that you drawn me with. To my brothers and sister, thank you for your warm encouragement . Thank you to my in laws who have been great supporters from the first day of

announcing the idea of a Ph. D. in nuclear physics.

Last, but not least, I would like to thank my husband, Mustafa Halawani, who has been there for me from the start, Without whom none of this would have been possible. I can't wait to see you on the other side of the world, my love.

ABSTRACT

Fast-beam collinear laser spectroscopy experiments on the exotic rubidium and gallium isotopes have been performed at the ISAC radioactive ion beam facility at TRIUMF.

The neutron-rich rubidium isotope chain up to $N=61$ is investigated. Specifically, the neutron-rich ^{98}Rb isotope has been studied for the investigation of shape coexistence. Two long-lived nuclear states in ^{98}Rb have been clearly observed for the first time: a low-spin state, assigned a spin of $I = 0$, and a high-spin state. The high-spin state is tentatively assigned a spin of $I = 3$ based on this work in combination with gamma decay results. There is no evidence of deviations from the behavior of the changes in the charge radii. The hyperfine structure of the neutron-rich ^{99}Rb was observed. Both suggested spins $I = \frac{5}{2}$ and $I = \frac{3}{2}$ were based on both experimental results of the stable isotopes ^{85}Rb and ^{87}Rb . Neither spins can be ruled out.

The neutron-deficient gallium isotopes down to $N=32$ have been measured via laser spectroscopy. Their hyperfine structures and isotope shifts are reported in this work. The magnetic dipole and electric quadrupole moments of ^{65}Ga and ^{67}Ga were measured for the first time, and were for ^{65}Ga : $\mu = +1.758(5)\mu_N$ and $Q_s = +0.226(14)b$ respectively. For ^{67}Ga the measured moments were $\mu = +1.849(5)\mu_N$ and $Q_s = +0.207(13)b$. Analysis of the trend in the neutron-deficient charge radii illustrate that there is no evidence for deformations from the behaviour in the gallium in the $N = 32$ region. With regard to the observed ^{62}Ga , its isotope shift and its charge radius could not be determined but were narrowed down, due to the low yield of

this isotope. A motivated discussion for a future investigation on ^{62}Ga is included. These measurements have been carried out along with the developments of new laser techniques: laser chopping and switching. These techniques were developed by the collinear laser spectroscopy group at TRIUMF to which the author contributed.

ABRÉGÉ

Nous avons exécuté des expériences sur des isotopes exotiques du Rubidium et du Gallium en utilisant la méthode de spectroscopie laser colinéaire sur des faisceaux rapides. Ces expériences ont eu lieu à ISAC (TRIUMF), un laboratoire pour la production de faisceaux de noyaux radioactifs. La série des isotopes riches en neutrons du Rubidium jusqu'à $N = 61$ a été étudiée. Particulièrement, l'isotope riche en neutrons ^{98}Rb a été étudié pour mettre en lumière la coexistence des différentes formes du noyau. Deux états nucléaires de longue durée de vie ont été observés pour la première fois: un état avec un spin nucléaire $I = 0$, ainsi qu'un état montrant un spin nucléaire plus élevé. Préliminairement nous avons assigné un spin nucléaire $I = 3$ à cet état, une décision basée sur les résultats de ce travail ainsi que sur les résultats en provenance de la spectrométrie gamma. Nous avons aussi mesuré la structure hyperfine de l'isotope riche en neutrons, ^{99}Rb . Les deux spins suggérés, $I = \frac{5}{2}$ et $I = \frac{3}{2}$, proviennent des résultats des études de ^{85}Rb et ^{87}Rb , deux isotopes stables. Ni l'un, ni l'autre est désirable.

Nous avons aussi étudié les isotopes déficients en neutrons du Gallium ($N = 32$ et plus élevé) à l'aide de la spectroscopie laser. La structure hyperfine et les déplacements isotopiques de ces isotopes seront présentés dans cette thèse. Le moment magnétique et le moment quadropolaire du ^{65}Ga et du ^{67}Ga ont été mesurés pour la première fois. Pour ^{65}Ga : $\mu = +1.758(5) \mu_N$ et $Q_s = +0.226(14) b$. Pour le ^{67}Ga les moments nucléaires sont $\mu = +1.849(5)\mu_N$ and $Q_s = +0.207(13)b$ Une analyse des déplacements isotopiques montre qu'il n'y a pas de changement prononcé de la

déformation dans cette région autour de $N = 32$. En ce qui concerne nos efforts pour mesurer le déplacement isotopique du ^{62}Ga , ainsi que son rayon de charge, aucun signal évident n'a été observé à cause de la faible intensité du faisceau. Une discussion sur la motivation pour des mesures futures du rayon de charge du ^{62}Ga est incluse dans le chapitre final de cette thèse.

Toutes les expériences mentionnées ci-haut furent faites en parallèle avec le développement de nouvelles techniques en spectroscopie laser colinéaire : L'utilisation d'impulsions laser très courtes combinée avec des changements rapides de fréquence laser. Ces techniques ont été établies par le groupe de spectroscopie laser de TRIUMF dont l'auteur est un membre.

TABLE OF CONTENTS

| | | |
|------------------|--|------|
| DEDICATION | | ii |
| ACKNOWLEDGEMENTS | | iii |
| ABSTRACT | | vi |
| ABRÉGÉ | | viii |
| LIST OF TABLES | | xiii |
| LIST OF FIGURES | | xiv |
| 1 | Laser spectroscopy in nuclear physics | 1 |
| | 1.1 Introduction | 1 |
| | 1.2 This work | 2 |
| 2 | Hyperfine structure and nuclear proprieties | 5 |
| | 2.1 Hyperfine structure | 5 |
| | 2.1.1 Fine and Hyperfine Interactions | 5 |
| | 2.1.2 Magnetic dipole moment | 8 |
| | 2.1.3 Electric quadrupole moment | 10 |
| | 2.1.4 Nuclear spin determination | 11 |
| | 2.2 Isotope shift | 12 |
| | 2.2.1 Mass shift | 12 |
| | 2.2.2 Field shift | 13 |
| | 2.2.3 Mean square charge radius | 14 |
| | 2.3 Essential experimental considerations | 15 |
| | 2.3.1 Atomic linewidth (Natural linewidth) | 15 |
| | 2.3.2 Power broadening of the spectral lines | 15 |
| | 2.3.3 Doppler broadening | 16 |

| | | |
|-------|---|----|
| 3 | The ISAC facility at TRIUMF | 17 |
| 3.1 | Production of radioactive isotopes at TRIUMF. | 17 |
| 3.2 | Collinear laser spectroscopy with fast beams (CFBS) | 18 |
| 3.3 | The CFBS beam line components | 19 |
| 3.3.1 | Radio Frequency Quadrupole (RFQ)- ion cooler and buncher | 21 |
| 3.3.2 | Charge exchange cell (CEC) | 23 |
| 3.3.3 | Light collection region (LCR) | 23 |
| 3.4 | Data acquisition system (DAQ) | 23 |
| 4 | Laser spectroscopy instrumentation and techniques | 28 |
| 4.1 | The titanium sapphire laser | 28 |
| 4.2 | Frequency stabilisation | 29 |
| 4.3 | The frequency doubler unit | 31 |
| 4.4 | Developed laser techniques | 34 |
| 4.4.1 | Laser chopping using an electro-optical modulator | 34 |
| 4.4.2 | Frequency switching | 35 |
| 4.4.3 | Integration with DAQ | 38 |
| 5 | Laser spectroscopy on neutron rich rubidium | 41 |
| 5.1 | Introduction | 41 |
| 5.2 | Experimental setup | 44 |
| 5.3 | Experimental Procedure. | 45 |
| 5.4 | Data analysis | 47 |
| 5.4.1 | Laser spectroscopy of ^{85}Rb and ^{87}Rb | 48 |
| 5.4.2 | Laser spectroscopy of ^{92}Rb | 51 |
| 5.4.3 | Spin determination of ^{98}Rb | 51 |
| 5.4.4 | Spin analysis of ^{98m}Rb | 53 |
| 5.4.5 | Spin analysis of ^{99}Rb | 56 |
| 5.5 | Conclusions | 60 |
| 6 | Laser spectroscopy of gallium isotopes | 62 |
| 6.1 | Introduction | 62 |
| 6.2 | Experimental setup | 65 |
| 6.3 | Data analysis | 67 |
| 6.3.1 | Laser spectroscopy of ^{69}Ga | 69 |

| | | |
|--------|---|----|
| 6.3.2 | Laser spectroscopy of ^{68}Ga | 70 |
| 6.3.3 | IS and mean charge radii of ^{67}Ga | 72 |
| 6.3.4 | IS and mean charge radii of ^{65}Ga | 72 |
| 6.3.5 | Measurements of ^{64}Ga and ^{66}Ga | 74 |
| 6.3.6 | Measurements of ^{63}Ga | 76 |
| 6.3.7 | Measurements of ^{62}Ga | 77 |
| 6.3.8 | Nuclear moment analysis | 77 |
| 6.3.9 | Changes in charge radii from two transitions | 78 |
| 6.3.10 | Extracting the changes in mean-square charge radii | 79 |
| 6.4 | Conclusions | 82 |
| 7 | Conclusions and summary | 84 |
| 7.1 | This work | 84 |
| 7.2 | Motivation for future work | 85 |
| | References | 89 |

LIST OF TABLES

| Table | page |
|--|------|
| 5-1 Summary of half-lives and yields of Rb isotopes from UC_x target. . . | 45 |
| 5-2 Hyperfine coefficients and the isotope shifts of ^{85}Rb and ^{87}Rb were measured from ^{92}Rb | 50 |
| 5-3 Hyperfine coefficient of the high spin ^{98}Rb | 54 |
| 5-4 The possible spins $I = 3/2, 5/2,$ and $7/2$ hyperfine coefficients, A ratios, and χ_r^2 for ^{99}Rb | 57 |
| 5-5 The possible transitions in ^{85}Rb | 59 |
| 5-6 The possible transitions in ^{99}Rb | 60 |
| 6-1 Summary of half-lives and yields of Ga isotopes from ZrC target . . . | 65 |
| 6-2 Hyperfine coefficient values of ^{69}Ga | 70 |
| 6-3 Hyperfine coefficient values of ^{68}Ga | 71 |
| 6-4 Hyperfine coefficient values of ^{67}Ga | 72 |
| 6-5 Hyperfine coefficient values of ^{65}Ga | 74 |
| 6-6 Isotope shifts from ^{69}Ga | 75 |
| 6-7 Hyperfine coefficient values of ^{63}Ga | 77 |
| 6-8 Nuclear moments of $^{63,65,67}\text{Ga}$ | 78 |
| 6-9 Isotope shifts from ^{69}Ga in the 417 nm and the 403 nm transition lines | 79 |
| 6-10 Isotope shifts and changes in mean-squared charge radii from ^{71}Ga . . | 80 |

LIST OF FIGURES

| <u>Figure</u> | <u>page</u> |
|---|-------------|
| 2-1 Typical hyperfine level splitting | 8 |
| 3-1 The CFBS beam line in the low energy area of the ISAC-1 hall. | 18 |
| 3-2 The laser spectroscopy beam line components. | 20 |
| 3-3 The electric potential applied to the RFQ during the trapping and ejection modes. | 22 |
| 3-4 Pulse sequence for the MCS-DAQ system. | 25 |
| 3-5 Typical spectra for ^{92}Rb | 26 |
| 4-1 Main laser system for laser spectroscopy on gallium. | 29 |
| 4-2 Frequency stabilisation setup. | 30 |
| 4-3 The laser locking system | 31 |
| 4-4 The WAVETRAN external frequency doubler cavity | 32 |
| 4-5 The light path for light modulation | 37 |
| 4-6 Illustration of the synchronisation sequence of the RFQ, EOM and AOM. | 38 |
| 4-7 Schematic of the data-acquisition hardware | 39 |
| 4-8 A fluorescence spectrum of ^{206}Fr | 40 |
| 5-1 Isotope shifts of the ground states of rubidium isotopes from ^{87}Rb | 43 |
| 5-2 The measured hyperfine structure of rubidium isotopes in the $5s^2S_{1/2} \rightarrow 5p^2P_{3/2}$ transition. | 47 |
| 5-3 The fitted hyperfine structure of ^{85}Rb | 49 |

| | | |
|------|---|----|
| 5-4 | The laser chopping technique effect demonstrated on the high frequency multiplet of ^{85}Rb | 50 |
| 5-5 | The fitted hyperfine structure of ^{92}Rb | 51 |
| 5-6 | Hyperfine spectrum for ^{98}Rb | 52 |
| 5-7 | Typical spectra for ^{92}Rb | 53 |
| 5-8 | The mean square charge radius along the rubidium isotopes between N=50 and N=61 | 55 |
| 5-9 | The fitted hyperfine structure of ^{99}Rb using $I = 5/2$ | 56 |
| 5-10 | The fitted hyperfine structure of ^{85}Rb | 58 |
| 6-1 | The root-mean-square matter radii and $E(7/2^2)$ excitation energies of the gallium isotopes | 63 |
| 6-2 | Plot of the deformation parameter β against neutron number in zinc and germanium | 64 |
| 6-3 | The atomic transitions chosen in gallium for this experiment | 66 |
| 6-4 | The measured hyperfine structure of all gallium isotopes in the $^2P_{3/2} \rightarrow ^2S_{1/2}$ transition | 68 |
| 6-5 | The measured hyperfine structure of $^{66,68,69}\text{Ga}$ isotopes in the $^2P_{1/2} \rightarrow ^2S_{1/2}$ transition | 69 |
| 6-6 | The fitted hyperfine structure of ^{69}Ga | 70 |
| 6-7 | The fitted hyperfine structure of ^{68}Ga | 71 |
| 6-8 | The fitted hyperfine structure of ^{67}Ga | 73 |
| 6-9 | The fitted hyperfine structure of ^{65}Ga | 74 |
| 6-10 | The fitted hyperfine structure of ^{64}Ga | 75 |
| 6-11 | The fitted hyperfine structure of ^{66}Ga | 76 |
| 6-12 | The fitted hyperfine structure of ^{63}Ga | 76 |
| 6-13 | Changes in mean-square charge radii of the gallium isotopes. | 81 |

| | | |
|------|---|----|
| 6-14 | The measured changes in mean-squared charge radii of gallium isotopes between the neighbouring even-even germanium and zinc isotopes. | 82 |
| 7-1 | The uncorrected f_t and corrected F_t values for the 13 selected superallowed cases. | 87 |

CHAPTER 1

Laser spectroscopy in nuclear physics

1.1 Introduction

The investigation of nuclear properties over the full nuclear chart requires precise, sensitive, and versatile techniques. Few methods, however, are suitable for broad surveys not only for a large number of nuclides but also providing a significant amount of detailed information for each nuclide studied. One of these techniques is collinear fast beam laser spectroscopy (CFBS) providing access to some of the most fundamental properties of nuclear ground as well as long lived isomeric states.

Over the past decades, nuclear structure investigations have shifted to more and more short-lived isotopes which are less abundant in nature than those close to the valley of stability. This was possible due to the important role that the radioactive beam facilities such as ISAC at TRIUMF are playing. At those facilities these rare isotopes are produced and extracted in sufficient amounts using ever improving techniques for extracting and delivering clean radioactive ion beams to the experiments performing nuclear structure studies. For different elements, chains of isotopes with different yields can be produced using different target materials and ion sources.

Concerning CFBS, this method was developed to measure the hyperfine structure and the isotope shifts in order to extract information about nuclear spins, nuclear moments and changes in mean square charge radius. Using this high resolution laser spectroscopy technique, monochromatic photons from a laser can be tuned to

a specific frequency to match the energy of a specific atomic transition in order to excite the individual transitions in the atom. Once excited the atom will release a photon in order to return to its lowest energy state. By measuring the energies of these transitions one can determine the splittings of the fine states. CFBS is one of the leading techniques for the investigation of nuclear ground state properties for radioactive species. Hand-in-hand with the above mentioned improvements of radioactive beam production and yields, development of new measuring and detection techniques for the CFBS [1] allow now for many more exotic and less abundant nuclei to be investigated compared to the early days when CFBS spectroscopy was established in the early 80's of the last century.

1.2 This work

This thesis will report the contribution of the author while part of the collinear fast-beam spectroscopy group at TRIUMF. These contributions involve two main different scientific projects within the field of laser spectroscopy. These are:

- (i) the investigation of the deformation and configuration mixing (shape coexistence) in the neutron-rich rubidium isotopes, and
- (ii) laser spectroscopy on neutron-deficient gallium isotopes.

Both studies have been done at the ISAC radioactive ion beam facility at TRIUMF. The author provided detailed calculations for the expected scanning ranges for the specific isotopes, preparation of the experiments, participated in the experimental shifts while running the experiment, fully analyzed the data and extracted the nuclear results presented here. In addition, the author participated in experimental runs on magnesium and francium isotopes and worked on improvements on laser

techniques described in Chapter 4. All this work was done in collaboration with the present of the other members of the group permanently stationed at TRIUMF, Matt Pearson the principal investigator, Thomas Procter, Postdoc, and Allen Leary a master student from McGill.

For the neutron-rich rubidium studies, Chapter 5 will give an overview of the data on the latest neutron-rich rubidium experimental campaign on rubidium and present the analysis done for this thesis on the hyperfine structure and isotope-shift measurements of the neutron-rich isotopes between $A=92$ and $A=99$. The measurement of the ground state spin of ^{92}Rb , ^{98}Rb , and ^{99}Rb as well as the investigation of the isomeric state of ^{98}Rb will be discussed and magnetic dipole and electric quadrupole moments will be presented. The isotope shift data of the neutron-rich isotopes will be collated with those measured previously [2, 3].

For the gallium experiment, Chapter 6 will present first measurements for the charge radii of ^{65}Ga and ^{67}Ga , as well as the nuclear moments of ^{65}Ga . The gallium isotopes will be taken up again in the final chapter, where we present the motivation for measuring the charge radius of ^{62}Ga for unitarity test of the Cabibbo-Kobayashi-Maskawa (CKM) matrix [4]. In this chapter we will also report on a first attempt to measure the isotope shift of ^{62}Ga and show preliminary data for this isotope.

However before presenting the rubidium and the gallium measurements, we will, in Chapter 2, provide the underlying theory of the hyperfine structure and describe how to extract the nuclear properties. In Chapter 3, an overview of the ISAC facility at TRIUMF will be presented, and the CFBS technique will be described in detail. Chapter 4 will spotlight recent developments in the laser spectroscopy

instrumentation and novel techniques, such as, laser chopping, frequency switching, and their integration with the Data Acquisition system (DAQ).

CHAPTER 2

Hyperfine structure and nuclear proprieties

2.1 Hyperfine structure

Modern laser spectroscopy techniques allow high resolution measurements of atomic hyperfine structure to be performed. When performed across a series of isotopes of the same element the evolution of nuclear structure along this chain can be determined. This includes nuclear properties such as the spin \mathbf{I} , magnetic dipole moment $\boldsymbol{\mu}$, electric quadrupole moment \mathbf{Q}_s , and the change in the root mean square charge radius $\delta \langle r_{ch}^2 \rangle$.

2.1.1 Fine and Hyperfine Interactions

The atomic structure is usually studied by observing the atomic transitions of electrons between two energy states. This is achieved by detection of a photon that is emitted during the process of excitation and de-excitation of an electron between two states. The difference in the energies of two electronic states is determined from the energy of the photon required to excite such a transition. The fine structure is the splitting in energy of the atomic states, of order 10^{-5} to 10^{-4} eV, due to the different couplings of the individual electron spin, \mathbf{S} , with the orbital angular momentum, \mathbf{L} , forming the total electron angular momentum, \mathbf{J} .

Observations of a smaller splitting compared to the fine structure splittings were observed in 1891 by Michelson, Fabry, and Perot in 1897 [5]. The range of this splitting is of the order of 10^{-7} to 10^{-8} eV, hence the name *Hyperfine*. This splitting

is caused by the interaction energy between the nuclear electromagnetic moments and the fields generated by the atomic electrons at the nucleus.

The total angular momentum of the system is described by a resultant angular momentum, \mathbf{F} , of the atom, resulting from coupling the nuclear spin, \mathbf{I} , and the total atomic angular momentum, \mathbf{J} , where

$$\mathbf{F}=\mathbf{I}+\mathbf{J}. \tag{2.1}$$

The number of the hyperfine states for each \mathbf{I} and \mathbf{J} is ranging from $\mathbf{F} = \mathbf{I} + \mathbf{J}$ to $|\mathbf{I} - \mathbf{J}|$ in integer steps, where the number of split components in a given multiplet is $(2J+1)$ or $(2I+1)$, whichever is smaller. Each F-state will have a different energy depending on the electromagnetic interaction between the nuclear moments and the electromagnetic field produced by the electrons at the nucleus.

The hyperfine interaction splits the fine structure energy states due to the energy of the interaction. This splits each fine structure into $2\mathbf{J}(\mathbf{I} \geq \mathbf{J})$ or $2\mathbf{I}(\mathbf{I} < \mathbf{J})$ states. The interaction can be expressed in a multipole expansion of the nucleus potentials as,

$$V = V_{Monopole} + V_{Dipole} + V_{Quadrupole} + V_{Octupole} + \dots \tag{2.2}$$

From the selection rules of the electromagnetic interaction, the terms which contribute the most are the even electric multipoles and the odd magnetic multipoles. $V_{Monopole}$ determines the gross structure and is equivalent to the potential used in the Bohr model. The fine interaction is a perturbation on the higher order terms in 2.2 resulting in the hyperfine structure. V_{Dipole} is associated with the nuclear spin I while $V_{Quadrupole}$ is connected to the deformation from the spherical charge

distribution of the nucleus. The higher order terms have a small contribution to the hyperfine structure which can be neglected for this work.

The shift in the atomic energy levels due to the perturbations caused by the multipole k is given by ΔE . In general,

$$\Delta E_k(IJF, IJF) = (-1)^{I+J+F} \left\{ \begin{matrix} I & I & k \\ J & J & F \end{matrix} \right\} \times \begin{bmatrix} I & k & I \\ I & 0 & -I \end{bmatrix} \begin{bmatrix} J & k & J \\ J & 0 & -J \end{bmatrix}^{-1} A_k. \quad (2.3)$$

where, \mathbf{A}_k is the product of the matrix elements of the nuclear and electronic spaces with ($k \geq 1$). The $6j$ symbol in the curly bracket, $\{ \}$, controls the hyperfine structure through F . The $3j$ symbols in the square brackets, $[\]$, are related to the projection of the tensor operators into the nuclear and electronic spaces. The hyperfine structure coupling constants A and B are defined with respect to A_k [6].

In order for an electron to be excited from one of the F -states to another one in a higher orbital level, the angular momentum should be conserved by following the specific selection rules $\Delta F = \pm 1, 0$ but not the 0 to 0 transition due to angular momentum conservation. Figure 2-1 is an illustration of both the magnetic and quadrupole interactions in the hyperfine structure. In general, for a one electron system, the electric quadrupole contribution can be considered as a small correction compared to the splitting caused by the magnetic dipole moment.

The total observable energy from a hyperfine structure can be combined using the effects of the electric quadrupole and magnetic dipole moments as,

$$\Delta E_{HFS} = E_{FS} + \Delta E_1 + \Delta E_2, \quad (2.4)$$

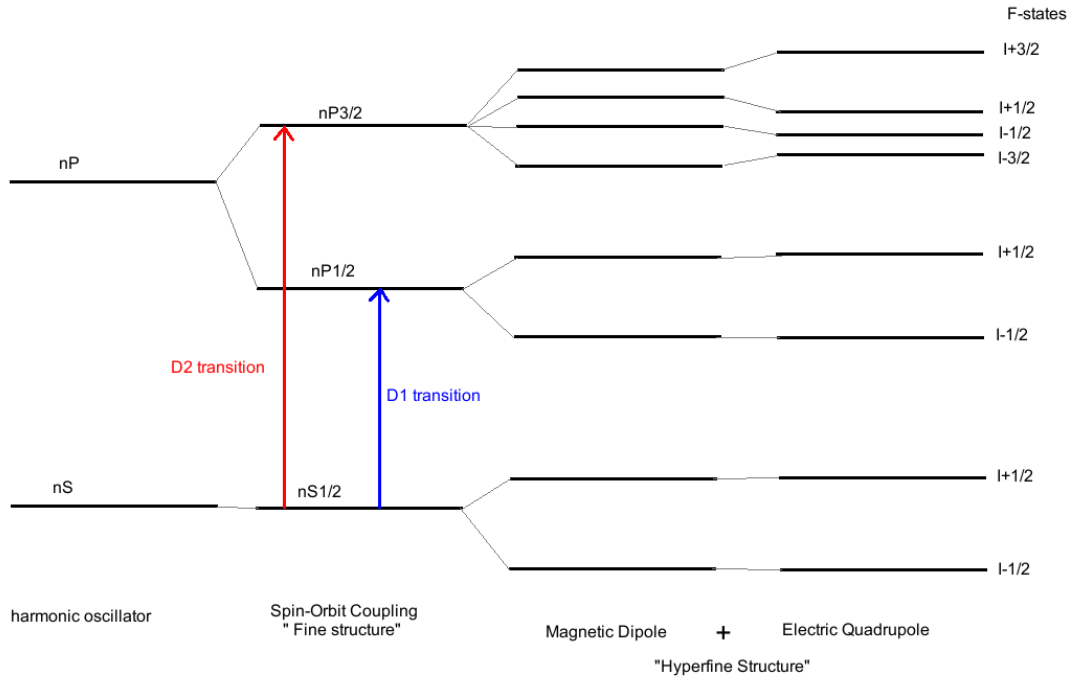


Figure 2–1: An illustration of level splittings in the hyperfine structure due to the magnetic dipole and electric quadrupole interactions for an alkali atom. This shows the D1 and D2 atomic transitions.

where E_{FS} is the fine structure transition centroid. ΔE_1 is the energy shift caused by the magnetic dipole interaction, while ΔE_2 is the energy shift due to the effect of the electric quadrupole interaction. These interactions will be discussed in more detail in the later sections.

2.1.2 Magnetic dipole moment

The interaction of the nuclear magnetic dipole moment, $\boldsymbol{\mu}$, with the magnetic field created by the orbital electrons at the nucleus, \mathbf{B}_e , produces the dipole term in

the hyperfine splitting [7]. The hyperfine energy created from the dipole interaction between the moment and the magnetic field [8] can be written as,

$$\Delta E_1 = \langle \boldsymbol{\mu} \cdot \mathbf{B}_e \rangle = -|\mu||B_e|\cos\theta. \quad (2.5)$$

where \mathbf{B}_e is the magnetic field and θ is the angle between \mathbf{I} and \mathbf{B}_e . The energy shift in the atomic state energies of each F caused by the magnetic dipole interaction is given by

$$\Delta E_1 = AC/2. \quad (2.6)$$

where C is given by

$$C = F(F + 1) - I(I + 1) - J(J + 1). \quad (2.7)$$

The hyperfine coefficient A can be explicitly written as :

$$A = \frac{\boldsymbol{\mu} \cdot \mathbf{B}_e}{\mathbf{I} \cdot \mathbf{J}}. \quad (2.8)$$

This shift can be experimentally measured via laser spectroscopy and is used to deduce A, since I and J are fixed for a given multiplet. The nuclear contribution from μ and I are constant for all atomic levels in a single isotope. Similarly, the atomic part presented by B_e and J is constant across all isotopes for a given transition.

Another consideration in determining the nuclear spin is the ratio of the A hyperfine coefficients as this ratio remains constant across an isotopic chain. So if this value has been measured for an isotope one can sometimes deduce the nuclear spin using the relation:

$$\frac{A_{upper}}{A_{lower}} = Constant. \quad (2.9)$$

Extraction of the nuclear magnetic moment, μ , directly from a measurement of the atomic hyperfine structure requires knowledge of the magnetic field created at the nucleus by the electrons. Assuming this field is constant across an isotope chain, this follows from Equation 2.8. As a consequence if the the ratio of A factor is known for one isotope, it is possible to calibrate the measurements to known values and calculate new magnetic moments. As long as the measurements have been performed on the same atomic transition, this removes the dependency of the magnetic field. The relation can be written as:

$$\frac{\mu}{\mu'} = \frac{IA}{I'A'}. \quad (2.10)$$

where μ , I , and A are the magnetic dipole moment, the spin, and the hyperfine coefficient of the isotope respectively, μ' , I' and A' are the magnetic dipole moment, the spin, and the hyperfine coefficient of the known reference isotope, respectively.

2.1.3 Electric quadrupole moment

The energy shift caused by the nuclear electric quadrupole moment, due to the coupling with the electric field gradient of the orbital electrons produced at the nucleus [8] is given by:

$$\Delta E_2 = \frac{B}{4} \frac{\frac{3}{2}C(C+1) - 2I(I+1)J(J+1)}{I(2I-1)J(2J-1)}. \quad (2.11)$$

where C is defined in Equation 2.7 and the hyperfine coefficient B is given by

$$B = eQ_s \left\langle \frac{\partial^2 V}{\partial^2 z} \right\rangle. \quad (2.12)$$

In Equation 2.12, $\left\langle \frac{\partial^2 V}{\partial^2 z} \right\rangle$ is the electric field gradient at the nucleus, e is the electron charge and Q_s is the spectroscopic nuclear quadrupole moment. In atomic systems

with either $I, J \leq 1/2$ the quadrupole contribution to hyperfine splitting vanishes. The spectroscopic nuclear quadrupole moment can be extracted using the measured B coefficient as well as Q_s of a reference isotope and assuming it is constant among the isotopic chain. The spacing between two successful F states is controlled by the Lande interval for hyperfine components,

$$\Delta E_{F,F-1} = AF. \quad (2.13)$$

In cases where either $I = 0$ or $J = 0$, there is no hyperfine splitting.

2.1.4 Nuclear spin determination

From hyperfine structure measurements it is sometimes possible to deduce the nuclear spin as well as the moments mentioned previously. This requires a well resolved hyperfine structure in addition to an accurate measurements of the transition frequencies. In this case the nuclear spin can be deduced from the atomic states' energy shifts as it also can be determined, in some cases, from the number of hyperfine structure transitions. However, sometimes it is difficult to extract all the hyperfine transitions from the spectrum. In some cases the relative intensities of the spectral lines can be used to extract the spin since the intensity of each transition depends on the nuclear spin I, J, and F of the involved atomic states. These intensities are expressed using a Wigner $6j$ symbol of the coupling of the angular momenta in each transition [9]:

$$Intensity = (2F_{lower} + 1) (2F_{upper} + 1) \left\{ \begin{array}{ccc} F_{lower} & F_{upper} & 1 \\ J_{upper} & J_{lower} & 1 \end{array} \right\}. \quad (2.14)$$

2.2 Isotope shift

The isotope shift (IS) is defined as the difference in the centroid frequencies of a given atomic transition between two different isotopes, with atomic masses A , and A' and is given by

$$\delta\nu^{AA'} = \nu^{A'} - \nu^A. \quad (2.15)$$

This shift is due to the effects of the nucleus on the atomic energy levels, where changes in the nuclear charge distribution and volume are involved. This shift can be divided into two different terms, the mass shift (MS) and the field shift (FS).

$$\delta\nu_{IS}^{AA'} = \delta\nu_{MS}^{AA'} + \delta\nu_{FS}^{AA'} \quad (2.16)$$

where $\nu^{A'}$ and ν^A are the centroid frequencies of the same atomic transition in A and A' isotopes.

2.2.1 Mass shift

The mass shift is due to the changes in nuclear recoil kinetic energy between two isotopes, hence it is related to the finite nuclear mass effect. This shift in the frequency of the atomic transition between the two isotopes, this change is stated by,

$$KE = \frac{m_A - m'_A}{2m_A m'_A} \left(\sum_i \mathbf{P}_i^2 + 2 \sum_i \mathbf{P}_i \cdot \mathbf{P}_j \right) \quad (2.17)$$

where m_A and m'_A are the masses of the isotopes, \mathbf{P}_i is the momentum of the i th electron in the atom. The first term in equation 2.17 gives the shift in energy levels for an atom with reduced mass and is referred to as the normal mass shift (NMS)

which can be defined in the following way [10]:

$$\delta v_{NMS}^{AA'} = \frac{m_e \delta A}{AA'} v \quad (2.18)$$

with m_e being the electron mass and $\delta A = A' - A$. The second term in equation 2.17 gives the specific mass shift (SMS) which represent a sum over all momenta correlations between pairs of electrons. It is also proportional to $\delta A/AA'$. The total mass shift can be expressed as,

$$\delta v_{MS}^{AA'} = \delta v_{NMS}^{AA'} + \delta v_{SMS}^{AA'}. \quad (2.19)$$

2.2.2 Field shift

The change in the extent of the nuclear charge distribution due to the change of neutrons inside the nucleus is referred to as the field shift (FS). Those tiny changes in the size of the nuclei still have effects on the atomic transitions. This effect can be illustrated by looking at a nucleus with an electron less bound than an nucleus with a finite charge distribution in the electrostatic electric field from the electrons [11]. If the electrostatic nuclear field to be considered as a perturbation for the coulomb potential of a point charge, then change in the electron energy levels can be expressed by

$$\Delta E = -e \int \left(\phi(r) - \frac{Ze}{4\pi\epsilon_0} \right) \Psi^2(r) dV \quad (2.20)$$

Where $\phi(r)$ is electrostatic nuclear field, $\Psi(r)$ is the electronic wavefunction. For an s-state ($l = 0$) electron, the wavefunction is independent of the angular part and presents only a radial dependence. Considering a non-zero probability of finding s-electrons inside the nucleus, and the nuclear size being much smaller than the atomic

radius, the radial wavefunction remains constant and equation 2.20 is reduced to contributions from the nucleus,

$$\Delta E = Ze^2 |\psi(0)|^2 \langle r_{ch}^2 \rangle, \quad (2.21)$$

where $\psi(0)$ is electronic charge density at the origin and $\langle r^2 \rangle$ is the mean-square charge radius and defined as,

$$\langle r_{ch}^2 \rangle = \frac{\int_0^\infty \rho(r) r^2 dV}{\int_0^\infty \rho(r) dV}, \quad (2.22)$$

with ρ being the charge density of the nucleus. For two isotopes A and A' the field shift due to this change in energy is given by

$$\delta v_{FS}^{AA'} = \frac{Ze^2 \Delta |\Psi(0)|^2 (\langle r_{ch}^2 \rangle)^{AA'}}{6h\epsilon_0} \quad (2.23)$$

where $|\Delta\Psi(0)|^2$ is the change in the electron density at the nucleus between the two atomic states, and $(\langle r_{ch}^2 \rangle)^{AA'}$ is the change in the nuclear mean square charge radius.

2.2.3 Mean square charge radius

In order to obtain the change in the mean square charge radii from the measured isotope shift, the mass shift is subtracted, where the overall isotope shift can be written as:

$$\delta v_{IS}^{AA'} = K_{MS} \frac{m_A - m'_A}{m_A m'_A} + F_{el} \delta \langle r_{ch}^2 \rangle^{AA'}. \quad (2.24)$$

K_{MS} is the mass-shift factor and F_{el} is the field-shift factor [11]. These factors are unique for each atomic transition. Hence, if the isotope shifts have been measured for the isotope chain and if F_{el} is known one can determine the change in the mean

square charge radii using equation 2.24 . This method will be used in chapter 4 and chapter 5 .

2.3 Essential experimental considerations

2.3.1 Atomic linewidth (Natural linewidth)

An associated homogeneous linewidth to the excited atomic state known as the natural linewidth, is due to the uncertainties in its energy and lifetime. Using the uncertainty principle, $\Delta E.\Delta t \approx h$ and taking the lifetime to be τ , the natural linewidth can be written as

$$\Delta\nu = \frac{\Delta E}{h} = \frac{1}{2\pi\tau} = \frac{\Gamma_0}{2\pi} \quad (2.25)$$

where Γ_0 is the total decay rate of the atomic state. This natural linewidth of the transition contributes to the full width at half-maximum (FWHM) associated with the Lorentzian line shape distribution.

2.3.2 Power broadening of the spectral lines

The interaction of the radiation field with the atomic system causes transitions between the lower and upper states at a certain frequency. In addition to this emission there is a stimulated emission induced by the laser photons. A certain frequency value, called saturation intensity [12], the populations in the two involved states will be equal. The saturating laser intensity I_s is given by :

$$I_s = \frac{h\pi\nu_0^3\Gamma_0}{3c^2}. \quad (2.26)$$

An increase in the laser power leads to an increase in the rate of the stimulated emission in the excited state, which effectively shortens the lifetime of the state. This

mechanism leads to a broadening of the line shape, causing a loss in the resolution and a lowering of the transition rate.

$$\Gamma = \Gamma_0 \sqrt{1 + \frac{I}{I_s}}. \quad (2.27)$$

In order to manage the power broadening the laser power should be set below the saturation value for the atomic transition, though enough to observe the atomic transitions.

2.3.3 Doppler broadening

Doppler broadening is the line width related to the thermal velocity spread of the atoms. Atoms moving with velocities relative to an observer will have frequencies Doppler-shifted with respect to an atom at rest. This can be described in terms of the Doppler width for a gas of thermal particles with resonance frequency ν_0 [13] given by

$$\delta\nu_D = \nu_0 \left(\frac{8kT \ln 2}{m_A c^2} \right)^{(1/2)}. \quad (2.28)$$

Where k is the Boltzmann constant and T is the absolute temperature of the atoms. Depending on the mass and temperature the Doppler broadening can be of the order of GHz, and this can suppress the individual hyperfine peaks.

CHAPTER 3

The ISAC facility at TRIUMF

3.1 Production of radioactive isotopes at TRIUMF.

The radioactive Ion beams (RIB) used in this work were produced by the Isotope Separator and Accelerator (ISAC) facility at TRIUMF. TRIUMF is Canada's national laboratory for nuclear and particle physics. Owned and administered by 19 Canadian universities, the on-site physics programs all utilise primary proton beams from the world's largest cyclotron. The cyclotron is initially fed by a continuous beam of negative hydrogen ions (H^-). These ions are bunched, then injected vertically, and directly into its centre. They are then allowed to be circulated and accelerated around the cyclotron. In the extraction process, the negative hydrogen ions (H^-) are stripped using a $25\mu m$ thin carbon foil to produce positive, proton beams (H^+). This extraction method allows simultaneous extraction of multiple proton beams at different locations and energies allowing up to four proton beams to be used in fundamental research, industrial application, and medical treatments simultaneously[14].

The ISAC facility is one of the proton beam users, served by a 500 MeV proton beam at currents up to $100\ \mu A$. In ISAC the proton beam is deflected onto a thick, (several cm long) ISOL (Isotope Separation On-Line) target operated at $\sim 2000^\circ C$. Within the target a multitude of different isotopes of many elements are produced by a variety of nuclear reactions. The reaction products leave the target foils and diffuse

into a transfer tube that is directly coupled to the ion source. Here the products are ionised before being extracted and sent to a two stage high resolution mass separator. The ion beam of interest is then directed along electrostatic beamlines into the ISAC experimental area.

The rubidium and gallium isotopes used for the study presented in this thesis were produced using different target materials. The neutron-rich rubidium atoms were produced using $10 \mu\text{A}$ protons impinging on a uranium carbide (UC_x) target. These atoms were surface ionised and accelerated to 20 keV prior to being sent to the experiment. For the studies on gallium a zirconium carbide (ZrC) target was bombarded with $40 \mu\text{A}$ of protons. The ion beam energy for this experiment was 30 keV. In general, for these type of experiments higher energies are preferred. However, practical limitations of the facility most commonly dictate the voltage used.

3.2 Collinear laser spectroscopy with fast beams (CFBS)

CFBS is a spectroscopy technique that is used with the radioactive ion beam (RIB) within ISAC hall at TRIUMF.



Figure 3–1: The CFBS beam line in the low energy area of the ISAC-1 hall.

The CFBS innovation within the laser spectroscopy techniques enables the observation and the study of rare and short lived radioactive nuclides such as the radioactive ion beams produced at TRIUMF [15]. One of the main issues with studying gaseous samples produced by evaporation was the velocity spread of its constituents due to thermal motion. This velocity spread leads to a Doppler broadening due to the velocities spread with respect to the light source. The observer then observes a Doppler broadened spectral line-width. On the other hand, looking for the best overlap of ion beam and laser beam is very important especially when dealing with rare and low yield radioactive elements. The CFBS beam's acceleration reduces its Doppler linewidth as $\Delta v = \frac{\Delta E}{mv}$. With Δv , the velocity spread of the beam, which is greatly reduced in accelerated beams.

3.3 The CFBS beam line components

The beam line is designed to collinearly overlap an ion/atom beam with laser light and observe resonant fluorescence. Radioactive ions produced in the ISAC target area are accelerated to the experiment where they are steered on to the path of a counter-propagating laser beam. The setup contains several steering electrodes to fine tune the ion beam and several Multichannel Plate detectors (MCPs) which are used to generate an electrical signal when struck by ions to check the beam transmission, efficiency, and to monitor the intensity of beams that are too weak to reliably measure on a Faraday cup. In addition these can provide timing information for bunched beams. The MCPs can be removed once calibrations are taken in this segment to allow the ions to fly to the next component. The ion beam is then

brought to the laser spectroscopy beam line as a continuous beam or sent to an off-axis beamline Radio Frequency Quadrupole (RFQ) Paul trap which is the first trap of the TITAN system (TRIUMF's Ion Trap for Atomic and Nuclear Science). The trap is held at a potential slightly below that of the energy of the ion beam. The ions are bunched within the Paul trap, reverse-extracted, and re-accelerated to the potential of the RFQ into the collinear laser setup for spectroscopic studies.

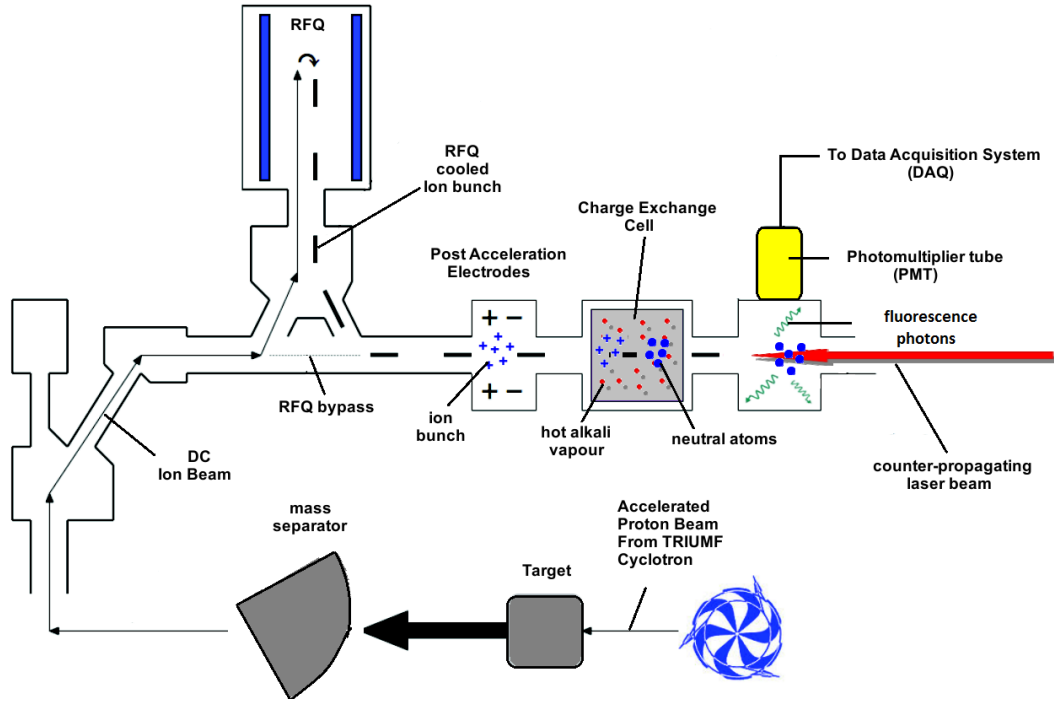


Figure 3-2: The laser spectroscopy beam line components.

In Figure 3-2 the laser spectroscopy beam line is shown starting with the continuous radioactive ion beam which can be used directly to investigate the electronic transitions or sent to the RFQ Paul trap where it is bunched, reverse-extracted, and re-accelerated towards the laser spectroscopy beam line. The ions then can

be neutralised by passing through a charge-exchange cell (CEC). The efficiency of neutralisation was monitored by the MCP which provides an estimate of the percentage of remaining ions and the neutralisation efficiency of CEC. In the rubidium experiment approximately 50% of neutralisation efficiency was achieved.

The atom/ion beam is collinearly overlapped with a counter-propagating laser beam in the interaction region. The laser light is set to a frequency that matches the energy of the electronic transition (in the centre of mass frame) under investigation and the ion/atom beam is then Doppler tuned onto resonance by adjusting the beam energy. The Doppler tuning voltage is applied to the charge-exchange cell. When on resonance with an electronic transition the electrons are excited to the higher configuration and then relax (governed by the natural lifetime of the transition), emitting fluorescent photons that can be detected by a photomultiplier tube (PMT). The Doppler tuning voltage is controlled via the data acquisition system and, in combination with the beam energy, laser frequency and photo-multiplier counts, the energies of the electronic transitions can be determined. After the interaction region the ions/atoms travel down the remainder of the beam line where any ion can be monitored off-axis by an MCP.

3.3.1 Radio Frequency Quadrupole (RFQ)- ion cooler and buncher

The RFQ ion cooler and buncher is the first trap in the TITAN system. It is located off axis to the CFBS beamline in order to facilitate use by both experimental beam lines. The RFQ is a segmented, gas filled, linear Paul trap used to accumulate, cool, and bunch the ions [16]. The ion beam has to be tuned into the RFQ and reverse-extracted and re-accelerated out to the CFBS beamline using deflection

electrodes. First, a voltage below the ion source's bias is applied to allow the beam to decelerate in order to trap them in a potential well within the RFQ. The ions are accumulated using this capture potential for a certain accumulation time which depends on the lifetime of the radioactive ion. The ions are collisionally cooled with an inert high purity buffer gas consisting of helium at 100 mbar which leads to a decreased energy spread of the low energy beam. An overview of the electric potential applied to the RFQ during the trapping and ejection modes is shown in Figure 3–3.

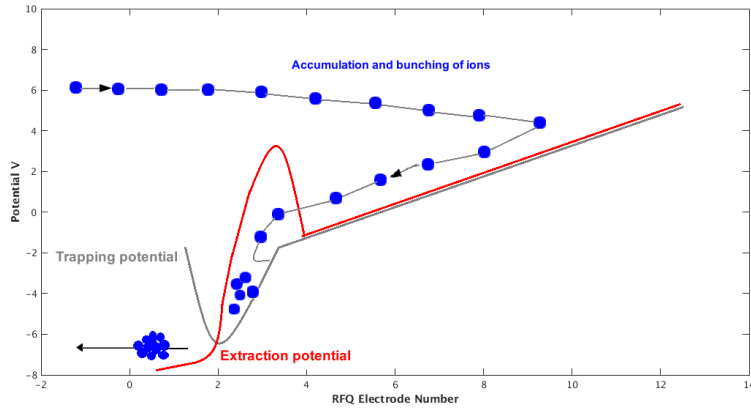


Figure 3–3: The electric potential applied to the RFQ during the trapping and ejection modes.

The bunched nature of the beam is more useful for our experiment. The ions are confined to a smaller region in space and energy so that they will be easier to observe and excite due to their higher density. The bunches have smaller energy spreads and so their time of flight (TOF) to the photomultiplier tube (PMT), where we acquire our data can be calibrated. The advantage of using the RFQ to cool and bunch our ion beam allows us to reduce our background by 4 to 5 orders of magnitude with respect to measurements using continuous ion beams.

3.3.2 Charge exchange cell (CEC)

The CEC produces an alkali vapour flow such as rubidium to neutralise the incoming ion beam. The alkali metal is placed in a heated reservoir. The incoming ion bunches collide with the heated alkali vapour where valence electrons are stripped from the alkali and neutralise the ions. The neutralisation efficiency is an important factor and during our experiment the charge exchange cell was operated at around 50% neutralisation efficiency to minimise the energy broadening of the atomic beam. This energy broadening can reduce the amount of nuclides which are doppler shifted into resonance with the laser. This would reduce the resolution of the measurements.

3.3.3 Light collection region (LCR)

The light collection region (LCR) is a region within the beamline that is designed to maximise the detection of the fluorescent photons. The atoms are observed within a housing that is 40 cm downstream of the charge exchange cell. This is blackened out to prevent external background photons to be reflected and is as close as possible to the charge exchange cell to limit the optical pumping effects without being affected by the alkali vapour. Within this housing unit there is an arrangement of spacers, filters and lenses used to optimise photon detection in front of the PMT.

3.4 Data acquisition system (DAQ)

The DAQ is a unique system that was developed at TRIUMF for the laser spectroscopy users. Its based on Multi-channel Scaler (MCS) software allowing the acquisition of a time, acceleration voltage correlated two dimensional spectrum. By gating the PMT signal with respect to the expected arrival of the bunch at the LCR, a significant background reduction of the order of 10^4 to 10^5 is achieved. A gate

placed around the time-of-flight (TOF) of the bunch arrival will optimise the signal-to-background ratio, but misplacing a hardware gate raises the possibility of losing a fraction of the resonant photons.

The voltage on the post-acceleration electrodes V_{acc} can be written as:

$$V_{acc} = V_0 + A_{100}(V_{DAC} + n\Delta V_{step}). \quad (3.1)$$

Where A_{100} is the KEPCO amplification factor (nominally 100), V_{DAC} is the DVM supplied control voltage set point, and ΔV_{step} the step size with n the step count used to scan the voltage. In order to obtain a voltage read-back for the DAQ system value for V_{acc} , a 10000:1 voltage divider is employed.

A novel system of triggers and Pulse Programmable Generator (PPG) is used. The full sequence is shown in Figure 3–4. The data acquisition and voltage scan cycle starts with the accumulation of ions in the RFQ. The RFQ accumulation and extraction trigger has been integrated into the DAQ system. This will ensure the same amount of atoms are available for each DAC step. A trigger is sent to the DAQ after the extraction potential is switched, which starts the data acquisition. At the start of the run, the PPG sets the timing structure within the MCS. In the rubidium work the observation time was set to 200 μs (2 μs per time bin and 100 time bins). The DAQ currently contains four MCS channels each with independent inputs but slaved to the same time structure. In general one input is used to bin PMT counts in time-bins down to 0.25 μs and the other to perform diagnostic measurements on the collected data.

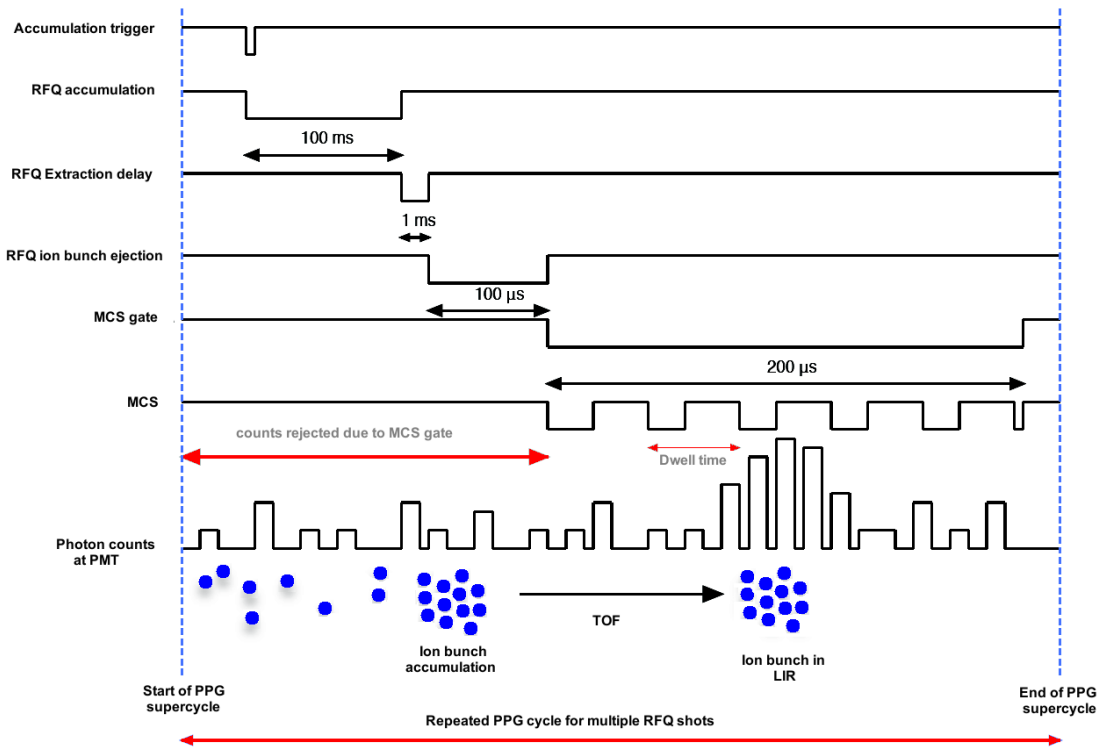
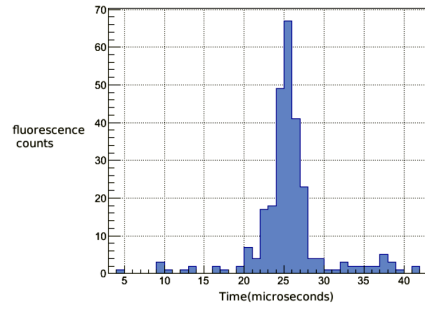
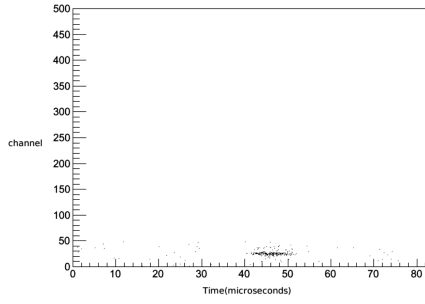
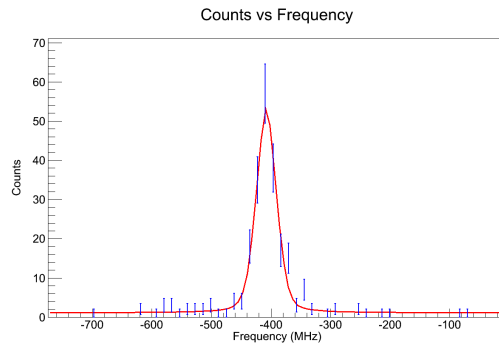


Figure 3-4: Pulse sequence for the MCS-DAQ system.



(a) *Two-dimensional on-line spectrum.*

(b) *Time-of-flight spectrum.*



(c) *Hyperfine spectrum.*

Figure 3–5: *A Typical spectra for ^{92}Rb with a single peak ($I=0$). ^{92}Rb was used as reference isotope in the rubidium experiment. A detailed description is provided in the text.*

Figure 3–5(a) shows the two dimensional on-line raw data directly at the end of the scan. The time and frequency structure plots are obtained by a projection of the counts onto the frequency and time axis, respectively. Figure 3–5(b) shows the time of flight (TOF) structure which was obtained by projecting the counts onto the frequency axis. The time information gained from the time of flight spectrum allow us to do a proper gate around the best time window. This can reduce the background noise without causing a peak suppression. The time of flight is expected to vary from one isotope to another depending on the mass, and this requires the time gate to be changed depending on the isotope under investigation. Figure 3–5(c) shows a fitted hyperfine spectrum for a ^{92}Rb isotope with spin $I = 0$. Using this method, gates can be applied post experiment in software and no information is lost due to a misplaced gate. A typical set of spectra for ^{92}Rb is shown in Figure 3–5. The two-dimensional spectra show the charge exchange cell bias in form of DAC steps and the time-of-flight (TOF) since RFQ extraction as time bins.

CHAPTER 4

Laser spectroscopy instrumentation and techniques

The laser system used in this work will be described. This includes a titanium sapphire (TiSa) ring laser, external frequency doubling cavity and associated optics. In addition several novel techniques developed during the period of this work will be described. These involve rapid switching of both the intensity and frequency of the light in order to reduce hyperfine pumping effects and hence increase the efficiency of the system.

4.1 The titanium sapphire laser

The laser system for the laser spectroscopy experiments consists of three individual parts. In Figure 4–1, the main laser system is shown. A Titanium:Sapphire (Ti:Sa) laser SolsTiS® system made by M^2 Lasers used in this thesis is a widely tunable, CW narrow linewidth laser, designed for use with a wide range of pump lasers. The Ti:Sa laser, has a very broad emission spectrum, and this property underpins the wide tuning range possible with SolsTiS, where Ti:Sa is a crystalline material, produced by substituting a small percentage of Al^{3+} ions with Ti^{3+} in an Al_2O_3 crystal host in a melt process. The Ti^{3+} ions are responsible for the laser emission in Ti:Sa., and the lasing tuning range achieved ranges from 670 - 1000 nm. The SolsTiS laser's ability to achieve ultra-narrow linewidths is a result of many innovative features incorporated into its electronic and mechanical design, including: a sealed, miniaturised, monolithic housing, and a compact laser cavity.

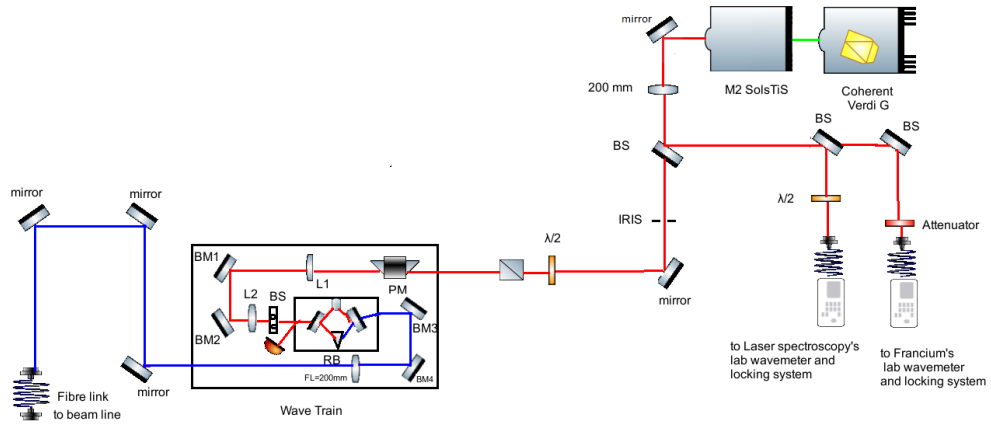


Figure 4–1: Main laser system for laser spectroscopy on gallium.

4.2 Frequency stabilisation

Frequency stabilisation over long term is a key point in the laser spectroscopy technique, since drifts in the frequency during scanning the optical spectrum transitions results in errors. The locking system described in Figure 4–1 consists of a frequency stabilised helium-neon (HeNe) laser and a scanning confocal Fabry-Pérot etalon with a 300 MHz free-spectral range (FRS)[17]. This setup is shown in Figure 4–2.

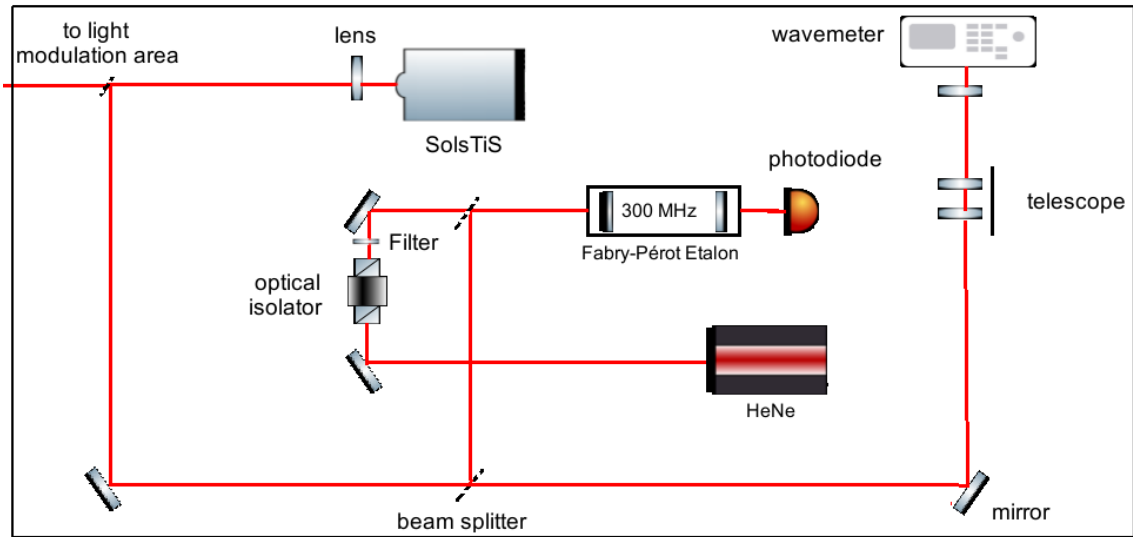


Figure 4-2: Frequency stabilisation setup.

The HeNe laser drifts by ± 0.8 MHz in 1 h and ± 1.2 MHz in 8 h [18], governed by the stability of the HeNe laser. Through scanning the cavity of the Fabry-Pérot etalon over 1.5 HeNe free-spectral ranges and by comparing the transmission fringes of the Ti:Sa and HeNe laser a feedback voltage is generated by a python script to stabilise the Ti:Sa laser. The location of the peaks with respect to a high voltage ramp that was applied to the etalon is read out. The program determines the positions of the peaks and calculates the difference. Based on that a correction voltage is fed back to the external scan input. Thus by keeping the distance between the two peaks constant over time, a long-term frequency stabilisation ≈ 5 MHz per day can be achieved. The peaks and the locking distances are similar to the ones shown in Figure 4-3 [19].

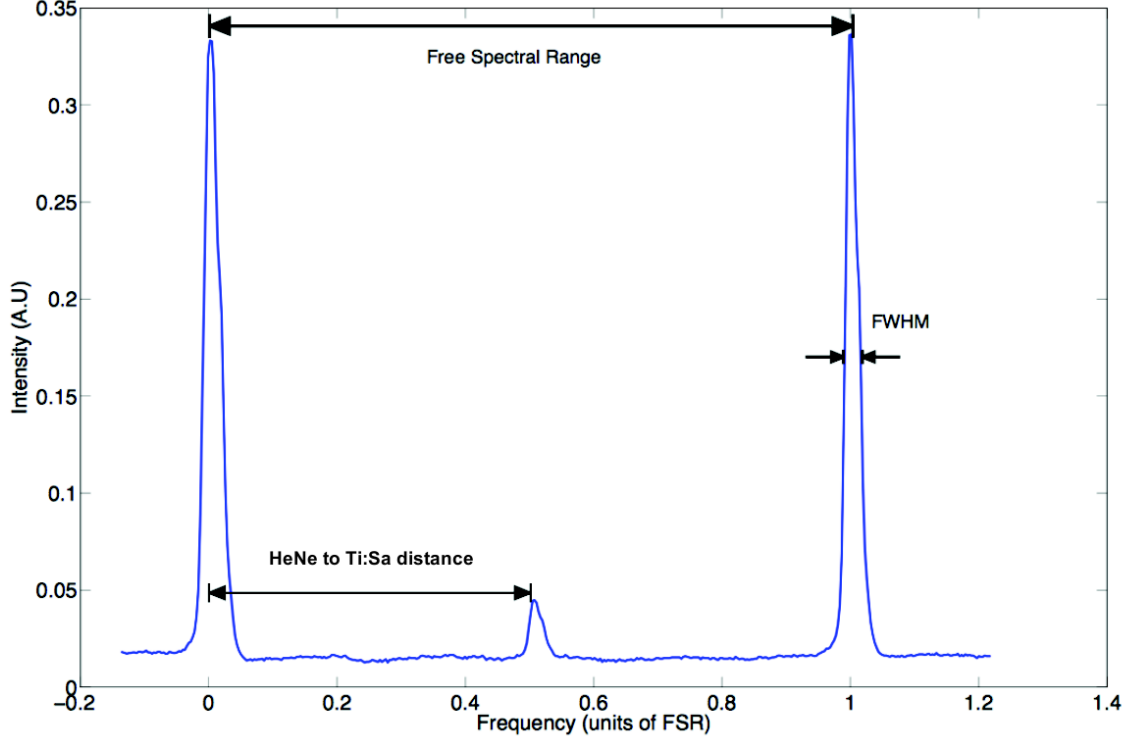


Figure 4–3: Laser locking system -transmission peaks for the reference HeNe and the Ti:Sa. The frequency axis is normalised in such way that the consecutive HeNe peaks that constitute a FSR are assigned.

4.3 The frequency doubler unit

In order to produce the second harmonic laser light used in the gallium experiment (403 nm and 417 nm), an external frequency doubler, WAVETRAIN® , from Spectra Physics was used to double the fundamental laser frequency (700 nm-1000 nm) output from the Ti:Sa laser. This apparatus is a ring cavity which is shown in Figure 4–4.

Cavity stabilisation is achieved using an active control method. This method is based on the Pound-Drever-Hall technique, which is aimed to measure changes in

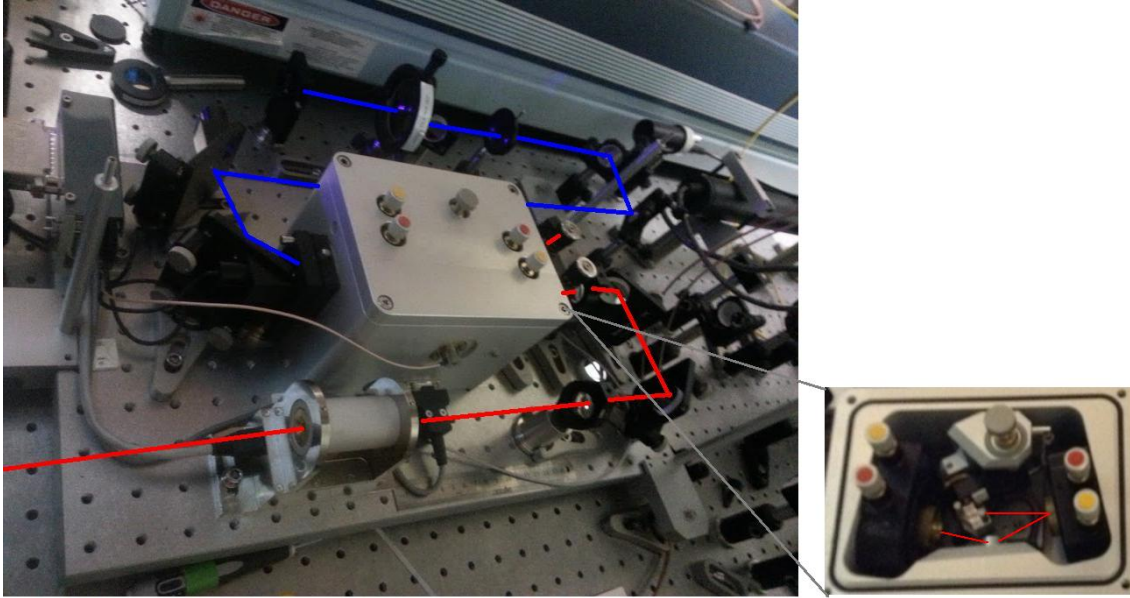


Figure 4-4: The WAVETRAN external frequency doubler cavity with the beam paths of the fundamental [Red] and doubled [Blue] light.

the derivative of the reflected light from the cavity. This technique adds sidebands to the fundamental laser beam and picking the reflected beam. The sidebands are added by the phase modulator which consists of electro-optic crystal. In order to improve the efficiency of the locking technique, and hence the cavity stability, the sidebands should be far enough from the resonance conditions inside the cavity in order to reflect. This reflected signal is mixed with the fundamental signal and by using phase sensitive detection, an error signal is obtained and fed back to a prism mounted on a piezo control, which adjusts the length of the cavity accordingly. This arrangement ensures the cavity stability. A detailed explanation of this technique can be found in [20]. The ratio of the harmonic power to the injected fundamental power, reaches its maximum value if the phase matching condition is fulfilled. This

means that the phase velocity of the harmonic wave equals the phase velocity of the fundamental wave in the material.

The cavity, along with its main optical components are shown in Figure 4–1. The fundamental input beam first passes the phase modulator (PM). The phase modulator adds sidebands to the fundamental beam. This is the optical part of the phase modulator assembly PMA that performs a phase modulation of the light wave. The PMA comprises the electro-optic crystals (2 KD*P crystals), the quartz oscillator, a fast photo diode for detection of the modulation signal as well as the electronics for the phase sensitive detection. The beam is then directed to the cavity by lenses L1 and L2 which are responsible for the correct mode matching of the input beam with respect to the resonator. Bending mirrors BM1 and BM2 are used for the alignment of the input beam into the cavity. The beam shifter (BS) allows very fine adjustments of the input beam by rotation of an AR-coated plane parallel plate. This plate BS together with L1 and L2 make the mode matching optics set. The ring cavity has the shape of triangle and the beam is deflected to the folding mirrors M1 and M2 by a prism. The fundamental beam passes through the non linear crystal(Lithium Triborate (LBO))and the second harmonic output leaves through M2. The major part of the fundamental which was not converted makes several rounds around in the cavity, which allows more power to be built, greatly improving the conversion efficiency. Failing to achieve perfect resonating in the cavity, part of the fundamental will leak and will be picked by a fibre couple and sent to the phase modulator module via an optical fibre. The error signal is then fed back to the piezo mount, which stabilises the cavity against vibrations. The

frequency doubler output is reshaped into a circular beam and then directed by BM3 and BM4 to another focusing lens before being directed to the CFBS beamline in the ISAC-I experimental hall via optical fibre. The use of a fibre ensures a near Gaussian mode at the beamline.

4.4 Developed laser techniques

Over the course of the last few years the laser spectroscopy group at TRIUMF has developed a series of techniques aimed at improving the sensitivity and versatility of the general scheme of collinear laser spectroscopy. These will be outlined individually below.

4.4.1 Laser chopping using an electro-optical modulator

In conventional CFBS atoms are excited by a continuous laser beam. The subsequent de-excitation by fluorescent emission can branch to other unwanted states. This 'hyperfine pumping' can alter the spectral intensities making them different from the theoretical predictions. The possibility of branching to other unwanted fine or hyperfine states can occur between the charge exchange cell and the light collection region, causing what is called 'hyperfine pumping' causing the hyperfine structure peaks to be suppressed.

In the CFBS beamline, neutralised atoms travel about 40 cm after the CEC to the LCR. To reduce hyperfine pumping, the exposure of these atoms to laser light must be minimised. This can be achieved by passing the laser light through an intensity modulating electro-optical modulator (EOM) to provide short photon bursts of high-power laser light delivered to the LCR. These burst durations can be controlled and set to the order of the hyperfine lifetime. The EOM, which is placed on

the laser path is controlled by a signal generator which allows modulation of the laser beam by using a reference square wave to trigger the switches between stopping and allowing the laser light to pass to the LCR. By calibrating the waveform generator's frequency each nuclide bunch travelling at $\approx 0.1\%c$ will only see one burst of light for a time of the order of 30 ns between the moment it is neutralised and the moment it passes the LCR. This limits the hyperfine transition cycles and eliminates the hyperfine pumping while preserving the peak intensity ratios. This technique can allow higher laser energies than in the classic CW setup as the average power the atom bunch receives is still low due to the short exposure time.

The high frequency intensity modulation technique was performed on the different radioactive Rb isotopes. For the rubidium experiment the light was pulsed at a repetition rate of 500 kHz which matches the 2 μ s flight time between the CEC and LCR. Each pulse has a duration of 30 ns, limited by the hardware, equal to the lifetime of the excited state of the transition.

4.4.2 Frequency switching

Rapid switching of laser frequencies was a different technique developed during this work to overcome the side effect of the high-frequency intensity-modulation technique. When the light pulses are travelling through the beamline they spend a significant amount of time without the atoms being in an interaction with the laser directly in front of the light collection region. We used this technique in a different experiment to study francium isotopes. Here, pulses arrived at a rate of 1 every 1.25 μ s (800 kHz). This means that the photon pulses will overlap with the atom beam at a certain location 4 times. Using pulses 80 ns long then the total overlap time of the

atoms with the laser is 320 ns. This means that most of the atoms are not excited as they pass the light collection region. In order to make use of most of the atoms arrive at the LCR a novel technique has been developed at TRIUMF. In this technique the photon pulses with different frequencies were delivered such that each atom bunch never interacts with two or more pulses of the same frequency. The repetition rate could be increased while limiting any possible hyperfine pumping that could happen while the light back towards continuous beam.

In this technique, the continuous laser beam is allowed to pass through an acousto-optic modulator (AOM), controlled by a varying RF signal to shift the frequency of the light equal to the RF. The switching rate of the RF is chosen to coincide with the electro-optical modulator(EOM) repetition rate such that each burst is of a different frequency. The effective, shifted frequency ν_{eff} of the laser is given by

$$\nu_{eff} = \nu_{laser} \pm 2 \times \nu_{AOM} \quad (4.1)$$

where ν_{laser} is the laser frequency before passing through the AOM and ν_{AOM} is the RF applied to the AOM at the instant the light passes through. The AOM frequencies are chosen so that the frequency was shifted by approximately 20 MHz apart. In order to separate the effective laser frequencies and to minimise off-resonant hyperfine pumping effects, the AOM frequencies are chosen such that the frequency shift exceeds the natural line width of the transition under investigation. The laser light was then passed through the EOM temporally modulating the intensity before delivery to the beam line. The laser path during frequency switching and intensity modulation techniques is shown in Figure 4-5.

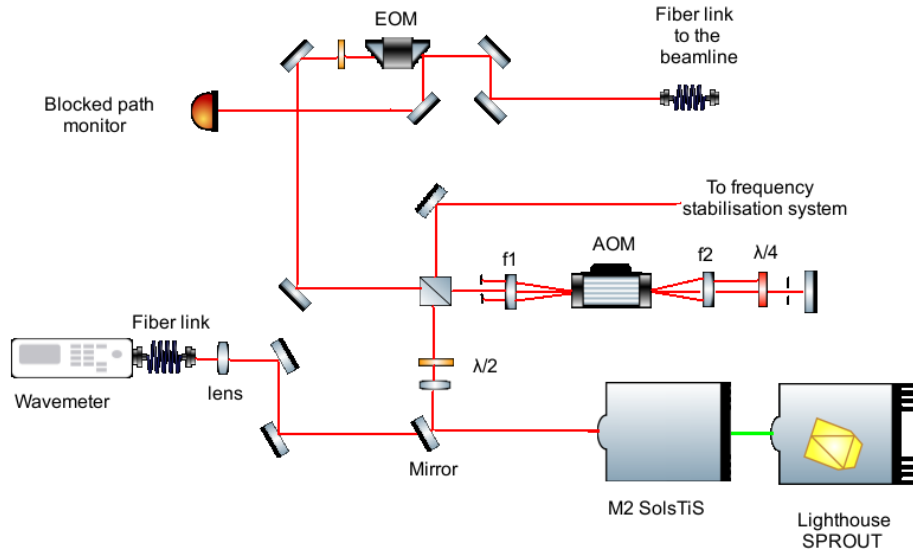


Figure 4–5: The light passes through an AOM for frequency switching and then through an EOM for intensity modulation.

In this test the rapid frequency switching technique provided an increase in efficiency of 50 – 60% while maintaining a comparable reduction in optical pumping. During the tests the power of each laser pulse was limited due to experimental constraints. In the future, larger pulse powers will further improve the experimental efficiency while minimising optical pumping effects. This technique was very successful for the francium experiment, but not required for the rubidium or gallium runs. This technique was first reported in [21].

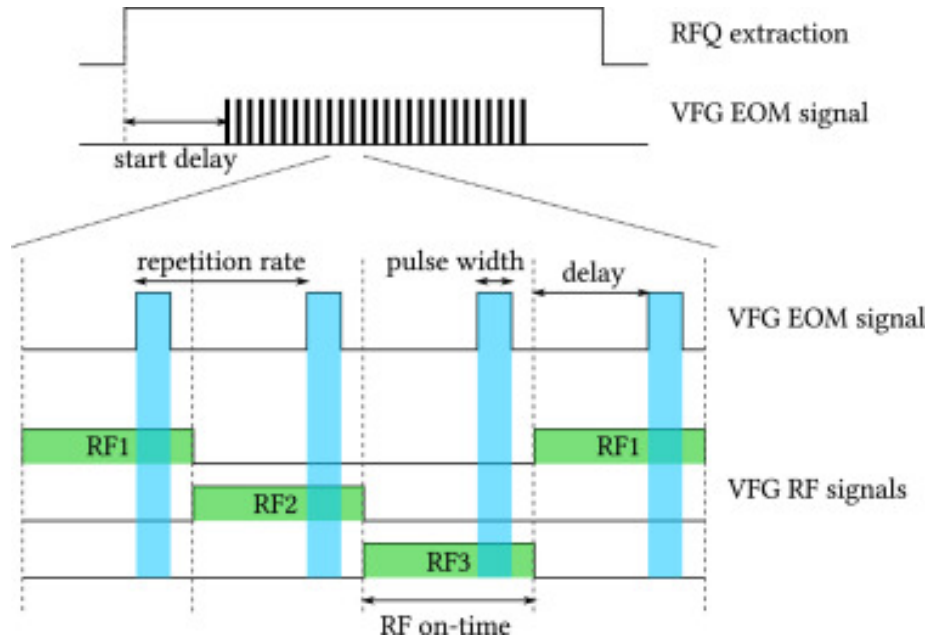


Figure 4–6: Illustration of the synchronisation sequence of the RFQ, EOM and AOM.

4.4.3 Integration with DAQ

For all these techniques, a synchronisation among the EOM, AOM and DAQ is crucial. An illustration of the synchronisation sequence of the RFQ, EOM and AOM is shown in Figure 4–6.

A schematic of the corresponding hardware is given in Figure 4–7. The hardware data acquisition system for performing the high-frequency intensity modulation and rapid frequency switching techniques is shown. The process starts with a constant trigger sent from a signal generator to the EOM to modulate the intensity of the laser light. The trigger signal is coincided with release trigger from the RFQ and delivered to the variable frequency generator (VFG) to switch the RF supplied to the AOM while the RFQ is in extraction mode. Logical on/off signals from the VFG

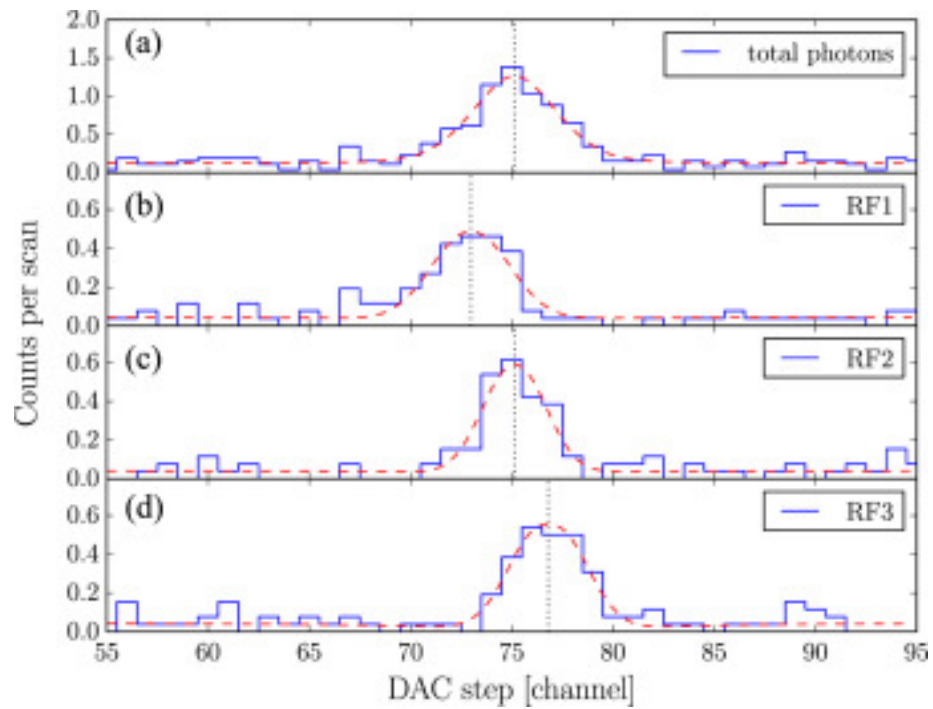


Figure 4-8: The fluorescent photons observed for the high spin hyperfine multiplet in ^{206}Fr for the unseparated DAQ channel (a) and separated according to the different AOM RF (b-d). The dashed lines correspond to the fitted peak centroid.

CHAPTER 5

Laser spectroscopy on neutron rich rubidium

5.1 Introduction

Shape coexistence is an interesting case in the microscopic behaviour of an atomic nucleus. It is possible for the nucleus to form stable configurations of different shapes at similar excitation energies, where significant energy gaps between the single particle levels at different deformations exist at the Fermi surface. Nuclei with coexistence of two different shapes on the excited structure exhibit strong E0 transitions between excited states [22]. The strength of an electric monopole transition [E0] between states of the same spin and parity, J^π is analogous to B(E2) or B(M1) values.

Using the microscopic-macroscopic Finite-Range Liquid-Drop Model (FRLDM), Möller et al. predicted in [23] the regions of the chart where multiple shapes may coexist at low excitation energy. There are several experimental observations that are related to shape coexistence, such as the large changes of the mercury charge radius; a large isomeric shift was measured in ^{185}Hg [24]. Experimentally, the observed signatures for the region with neutron-rich nuclei around $A=100$ are: (i) Sharp change in the trends of the root-mean-square (RMS) charge radius along the isotopic chain as shown in figure 5-1; (ii) Strong E0 transitions between low lying 0^+ states.

The rubidium isotope chain, with $Z = 37$, falls into the $A=100$ region of the chart. Laser spectroscopy investigations were performed on many of the commonly

accessible rubidium isotopes [25, 16]. Towards $A=100$ less nuclear structure information is known. Figure 5–1 shows the isotope shifts across the rubidium isotopes from $N=37$ to $N=61$. From this it can be seen that, away from any adapted atomic model for the atomic factors in equation 2.24, the smallest root mean square charge radius corresponds to the closed neutron shell at $N=50$ with a spherical nuclear shape. The isotopes from $N=39$ to $N=50$ show a considerable departure from sphericity with a definite change in the nuclear structure. Between $N=51$ and $N=58$ a rapid, nearly linear decrease in the isotope shift, reflects a linear growth in the RMS charge radius is observed due to neutrons fill the sub-shells. Between $N=59$ and $N=60$ a large decrease in the isotope shift representing a large decrease in the RMS charge radius is observed, an order of magnitude bigger than the one observed for the previous isotopes in the chain. This sudden jump indicates a strong deformation change. This can be seen in the quadrupole moment Q which is the largest of the neutron rich side of the rubidium chain [26]. For ^{98}Rb at $N=61$, the presented work investigates the behaviour of the RMS charge radius of ^{98}Rb ground state as well as its possible isomeric state.

Several E0 transitions within the region were identified from the decay measurements that was performed recently by the 8π spectrometer [27]. This achievement combined with the RMS charge radius measurements will guide the theoretical calculations to a better understanding of the contribution of various residual interactions.

Penning-trap mass spectroscopy performed on ^{98}Rb yielded no signs of an isomeric state in ^{98}Rb [28, 29]. A possible reason for the lack of observation could be due to the production rate of the isomer being considerably different to that of

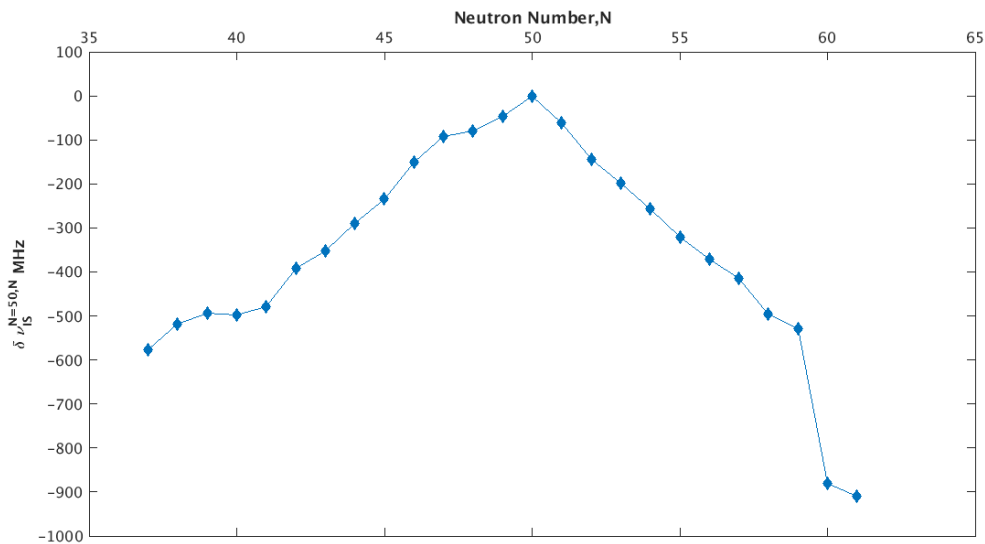


Figure 5-1: Isotope shifts of the ground states of rubidium isotopes with respect to ^{87}Rb . Data were taken from [16, 2]

the ground state or due to the close proximity of energy levels [30]. This work has extended the measurements of the root-mean-square charge radii of the neutron rich rubidiums to further investigate the deformation and configuration mixing within the region, and positively identified an isomeric state in ^{98}Rb .

Laser spectroscopy techniques are the key to precise and sensitive measurements to investigate the nuclear properties of ground and isomeric nuclear states. It allows extracting of the desired nuclear properties from the analysis of the hyperfine structures coefficients and the isotope shifts of the atomic transitions. Nuclear properties such as the nuclear spin I , magnetic dipole and quadrupole moments, and changes in the mean-square charge radius can be extracted [31].

In order to study the behaviour of the mean square charge radius [32], the measured spectroscopic quadrupole moment, Q_s , for a well-deformed nucleus is used

to extract the intrinsic quadrupole moment, Q_0 , through the relation

$$Q_0 = Q_s \frac{(I+1)(2I+3)}{I(2I-1)} \quad (5.1)$$

The nuclear static, $\langle\beta_2\rangle$, and the mean-square, $\langle\beta_2^2\rangle$, known as *Quadrupole deformations* can then be investigated, where the intrinsic quadrupole moment, Q_0 , can be related to the undeformed spherical nucleus mean-square radius, $\langle r_{sph}^2\rangle$, and the nuclear static, $\langle\beta_2\rangle$, via

$$Q_0 \approx \frac{5Z\langle r_{sph}^2\rangle}{\sqrt{5\pi}} \langle\beta_2\rangle (1 + 0.36(\langle\beta_2\rangle)) \quad (5.2)$$

Changes in mean-square quadrupole deformation, $\langle\beta_2^2\rangle$, can be extracted from the measured mean-square charge radii by

$$\delta\langle r_{ch}^2\rangle^{A,A'} = \delta\langle r_{sph}^2\rangle^{A,A'} + \langle r_{sph}^2\rangle \frac{5}{4\pi} \delta\langle\beta_2^2\rangle^{A,A'} \quad (5.3)$$

These deformation parameters can provide a measure to understand the nuclear deformation. The dynamic contribution is caused by the differences between the measured $\langle\beta_2\rangle^2$ and $\langle\beta_2^2\rangle$ values. This produces an unexpected increase in the mean-square charge radius. The dynamic deformation is usually denoted as a *softening of the core*, as the dynamic movement of the nucleus produces a larger time averaged charge radius. In the opposite case, a decrease will move the core into a more rigid system with a static shape deformation.

5.2 Experimental setup

The experiment on the exotic neutron-rich rubidium isotopes were performed at the ISAC radioactive ion beam facility at TRIUMF. The radioactive neutron rich

rubidium atoms were produced using up to 10 μA of 500 MeV protons from the TRIUMF cyclotron impinging on a uranium carbide (UC_x) target. The atoms were surface ionised then accelerated to 20 KeV. The beam was trapped in a gas filled linear Paul trap as outline in section 3.3, where the ions were cooled and bunched into the laser spectroscopy beamline. The yields of the neutron-rich rubidium isotopes of interest were measured before the experiment along with the half-lives are shown in Table 5–1.

Table 5–1: *Summary of half-lives and yields of Rb isotopes from UC_x target.*

| Isotope | Yield(ion/s) | $T_{1/2}$ |
|---------|-----------------|-----------|
| 98 | 7×10^5 | 114 ms |
| 98^m | 10^4 | 96 ms |
| 99 | 10^4 | 50.3 ms |
| 100 | 10^3 | 51 ms |

5.3 Experimental Procedure.

During the experiment, several scans were performed for each isotope, and were then individually analysed. Predictions of both the hyperfine peak energies and isotope shift were undertaken to assist the experiment. Isotope shifts of the first time measured isotopes were extrapolated from the known IS in [25, 33]. The hyperfine coefficients were also extrapolated from the A_L/A_U ratio of the previously measured rubidium isotopes of $\approx 40.3(1)$. A few scans for ^{87}Rb and ^{85}Rb , the stable isotopes were performed. ^{92}Rb was scanned in between every change of mass in the separator to detect any drifts in the centroids of the transitions. ^{92}Rb was used instead of ^{87}Rb

due to hardware limitations. For each scan, a data file of photon counts as function of the laser frequency was produced and used for the analysis. The analysis of the rubidium data was performed using a χ^2 minimisation technique. A fitting code in Root was used to fit the spectra. A simulated hyperfine structure was produced using predicted energy shifts with a fixed nuclear spin. The line shapes were simulated using Voigt profiles. The fitting parameters were the centroid for each transition, the background counts, and the full-width at half maximum (FWHM) was kept constant across all transitions in a single scan. The Lorentzian/Gaussian ratio, the intensities of the transitions and the hyperfine parameters, $A(P_{3/2})$, $A(S_{1/2})$, and $B(P_{3/2})$. $A(P_{3/2})$ was constrained to $A(P_{1/2})$ by a fixed known ratio among the Rb isotopes to be 40.3(1) to assist the fitting. The measured hyperfine structure of the rubidium isotopes in the D2 transition is shown in Figure 5–2.

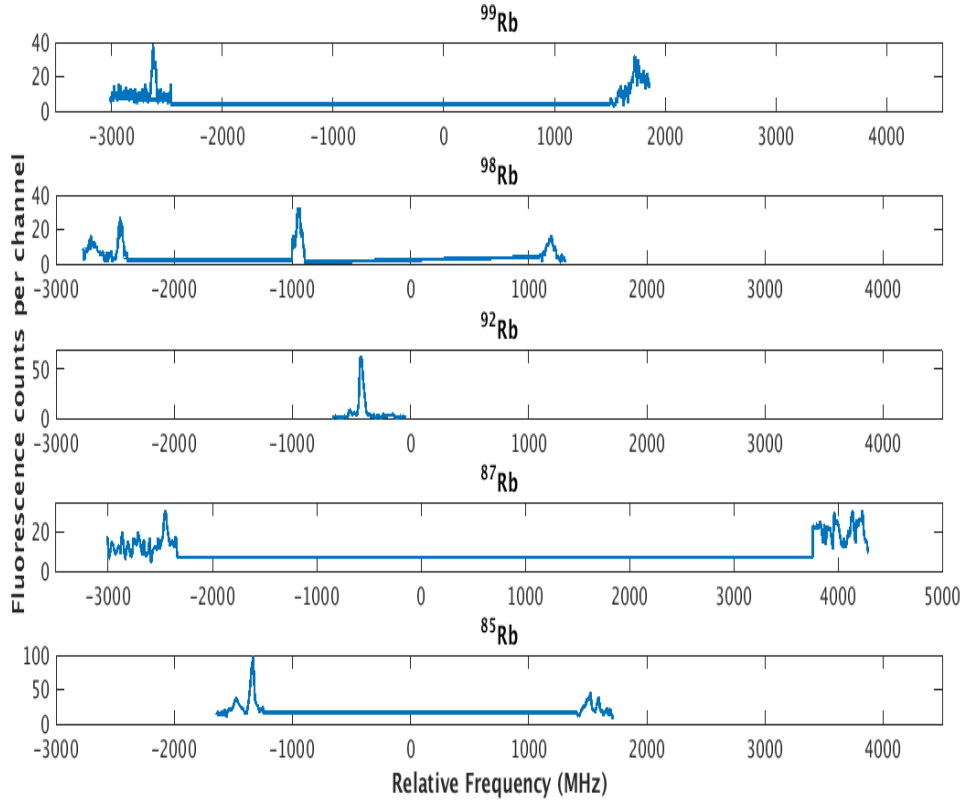


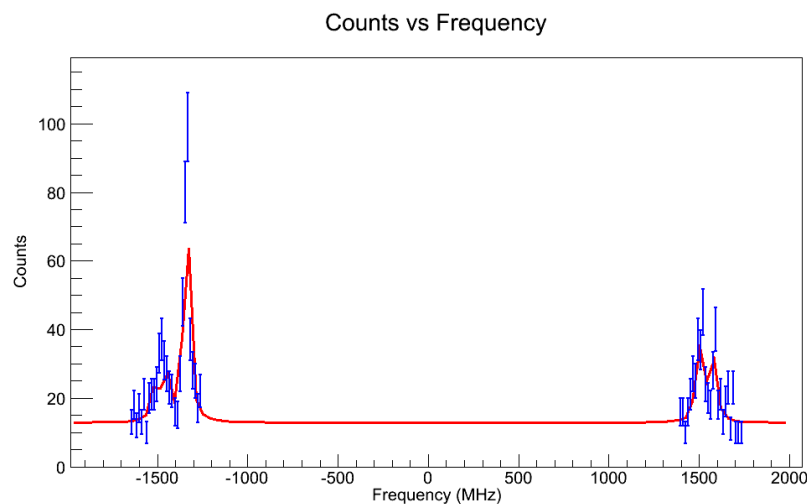
Figure 5–2: The measured hyperfine structure of rubidium isotopes in the $5s^2S_{1/2} \rightarrow 5p^2P_{3/2}$ transition.

5.4 Data analysis

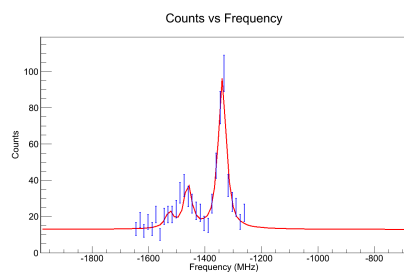
The rubidium A-hyperfine-coefficient ratio through the chain of the different isotopes is unique. The ratio of $\frac{A(5s^2S_{1/2})}{A(5p^2P_{3/2})}$ was measured to be $+40.3(1)$ [25]. This ratio, the χ_r^2 fitting routines, peak intensities and FWHM of the individual hyperfine peaks from the experimental values of ^{92}Rb experimental scans were used as constraints.

5.4.1 Laser spectroscopy of ^{85}Rb and ^{87}Rb

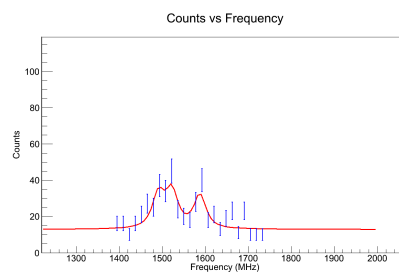
The known stable isotopes ^{85}Rb and ^{87}Rb of rubidium were investigated along with the series of the unknown isotopes. Isotope shifts were referenced to the stable ^{87}Rb with a nuclear spin $I = 3/2$. ^{85}Rb with spin $I = 5/2$ will be used in the analysis of ^{99}Rb which is predicted to have a nuclear spin $I = 5/2$. The fitted spectrum of hyperfine structure of ^{85}Rb is shown in Figure 5-3 .



(a) *The fitted hyperfine spectrum of ^{85}Rb .*



(b) *The fitted hyperfine spectrum - high spin frequency of ^{85}Rb .*



(c) *The fitted hyperfine spectrum - low spin frequency of ^{85}Rb .*

Figure 5-3: *The fitted hyperfine structure [solid red line] of ^{85}Rb , the stable isotope, is shown*

The isotope shifts of ^{85}Rb and ^{87}Rb were measured from ^{92}Rb and are shown below in Table 5-2. The hyperfine coefficients and the isotope shifts are in agreement with literature.

Table 5–2: Hyperfine coefficients and the isotope shifts of ^{85}Rb and ^{87}Rb were measured using ^{92}Rb . All quantities are measured in MHz

| A | This work | | Literature [16] | |
|-------------------------|-------------|-------------|-----------------|-------------|
| | 85 | 87 | 85 | 87 |
| $A(5s^2S_{1/2})$ | 1015.3(4.6) | 3420.1(2.1) | 1011.0(1.0) | 3415.9(2.0) |
| $A(5p^2P_{3/2})$ | 25.4(0.4) | 84.4(1.2) | 25.3(0.4) | 84.29(0.50) |
| $B(5p^2P_{3/2})$ | 25.3(3.7) | 12.3(1.2) | 21.4(4.0) | 12.2(2.0) |
| $\delta\nu_{IS}^{92,A}$ | -239.5(1.3) | -319.6(3.3) | -240.3(5.4) | -320.4(5.2) |

The laser chopping technique was used on several scans during this rubidium experiment. The effect of the intensity modulation on the high frequency multiplet of ^{85}Rb is shown in Figure 5–4. A reduced intensity and a change in the peak shape occurs due to reduction in the hyperfine pumping effect. Relative intensities for the modulated spectrum are within agreement with the calculated ones from equation 2.14.

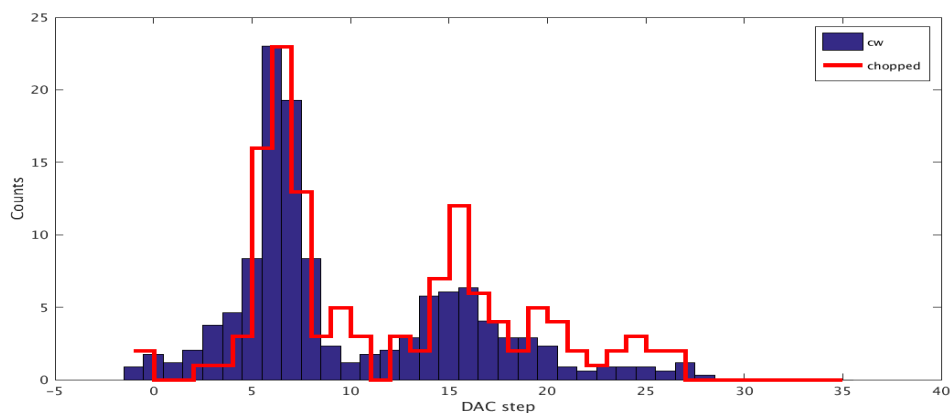


Figure 5–4: The laser chopping technique effect demonstrated on the high frequency multiplet of ^{85}Rb .

5.4.2 Laser spectroscopy of ^{92}Rb

^{92}Rb was used as a frequency reference. It is a hyperfine structure free isotope with nuclear spin $I=0$. The FWHM can be used while investigating the unassigned nuclear spin of the ground state of ^{98}Rb . The fitted hyperfine structure is shown in Figure 5-5.

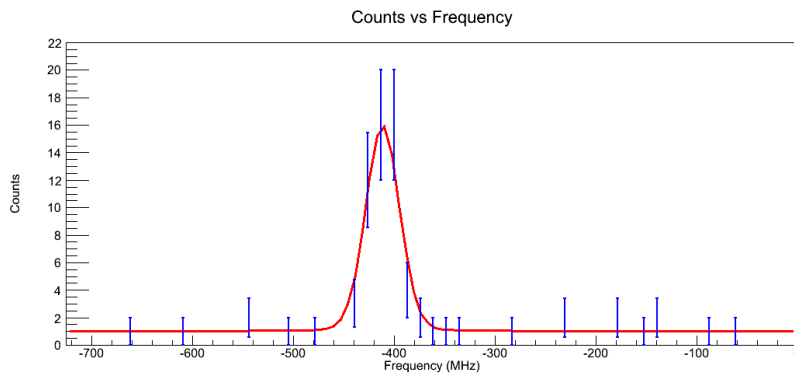


Figure 5-5: The fitted hyperfine structure [solid red line] of ^{92}Rb .

The structure is fitted with a single Voigt peak as described earlier with FWHM of approximately 35 MHz. This FWHM and the Voigt profile properties will be used while for the spin assignment of ^{98}Rb . The isotope shift from the stable isotope ^{87}Rb was measured to be $\delta\nu_{IS}^{87,92} = -319.6(3.26)$ MHz.

5.4.3 Spin determination of ^{98}Rb .

Prior this experiment, there was a tentative assignment of (0,1) for the spin of ^{98}Rb . There was no mention of an isomeric state. In [34] two long lived nuclear states of ^{98}Rb have been postulated. One has a low spin (LS) and had been assigned to spin $I=0$ in [25]. The high spin (HS) state was unobserved prior to this work. However, a gamma decay experiment had assigned a high spin $I = 3^+$ to be the ground state.

During the latest neutron-rich rubidium experiments, the laser spectroscopy group at TRIUMF observed two distinguishable nuclear states shown in Figure 5–6 [30].

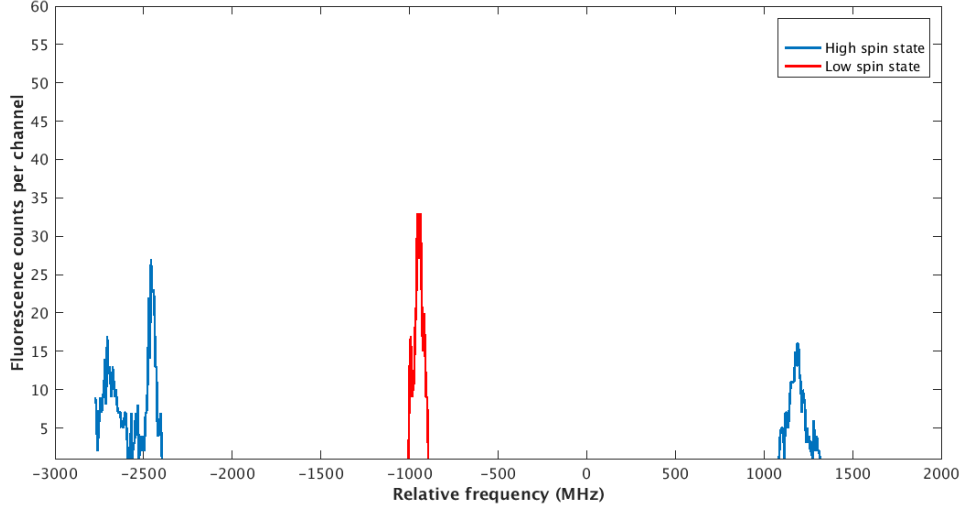
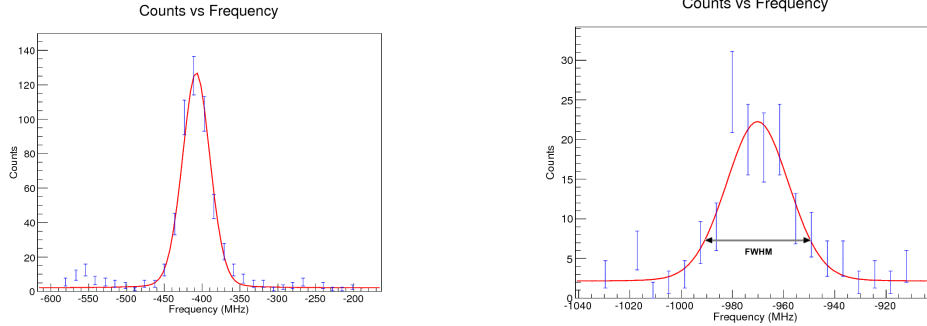


Figure 5–6: *Hyperfine spectrum for ^{98}Rb , measured on the $D2$ transition, showing the two observed nuclear states. The low-spin state $I = 0$ [red] and each side of the high-spin state $I = 3$ [blue] were individually scanned.*

The two states of the ^{98}Rb isotope have been investigated intensively during the last experiment on the neutron-rich rubidium isotopes. One state is fitted with a single Voigt peak with FWHM of approximately 35 MHz as shown in Figure 5–7. Both figures shown are from scans with chopped laser. This FWHM and the properties of the Voigt profile for the ^{98}Rb ground state were similar to other $I = 0$ states such as ^{92}Rb , excluding the spin $I = 1$ to be the ground state. An average of $\text{FWHM} \approx 35\text{MHz}$ was extracted in both cases. This was assigned early via laser spectroscopy measurements [16]. A slightly narrower hyperfine peak was noticed in the ^{98}Rb ground state due to the mass difference. The isotope shift of this low spin



(a) The fitted hyperfine spectrum of ^{92}Rb . $\text{FWHM} \approx 35\text{MHz}$ averaged from the ^{92}Rb .

(b) The fitted hyperfine spectrum of ^{98}Rb low spin state $I=0$.

Figure 5–7: Typical spectra for ^{92}Rb with a single peak ($I=0$) and a ^{98}Rb ground state. Detailed information is provided in the text.

state was measured to be $\delta\nu_{IS}^{92,98LS} = -590.1(0.9)\text{MHz}$, this IS was also in agreement with the literature [16].

5.4.4 Spin analysis of ^{98m}Rb

The high spin state was proposed in [34] to have a spin of $I = 3$ or $I = 4$. The high spin $I = 3$ has been suggested to be the ground state via decay spectroscopy [35]. During the experiment presented here two clearly distinguishable nuclear states were observed and the optical spectra obtained are shown in Figure 5–6. The measured hyperfine A and B coefficients and isotope shifts (relative to ^{92}Rb) of the high spin observed states in ^{98}Rb are shown in Table 5–3. The coefficients were extracted from the hyperfine structure using fixed angular momentum coupling estimates and the ratio of $\frac{A(2S_{1/2})}{A(2P_{3/2})} = +40.3(1)$. Constraints added to this fitting routines are relative peak intensities calculated by angular momentum couplings obtained from equation 2.14 and FWHM of individual hyperfine peaks from the experimental values

Table 5–3: *Hyperfine coefficient of the high spin ^{98}Rb*

| Spin I | χ_r^2 | A($5s^2S_{1/2}$)(MHz) | A($5p^2P_{3/2}$)(MHz) | B($5p^2P_{3/2}$)(MHz) | $\delta\nu_{IS}^{92,A}$ (MHz) |
|--------|------------|-------------------------|-------------------------|-------------------------|-------------------------------|
| (3) | 0.98 | 1108.5(0.6) | 27.51(0.07) | 134.7(2.7) | - 602.1(1.2) |
| (4) | 1.02 | 864.3(0.5) | 21.45(0.06) | 157.5(3.0) | -546.8(1.2) |

of the ^{92}Rb experimental scans. Reduced chi squared, χ_r^2 , values for I=5 and above along with inconsistent values for the ratios of fitted A hyperfine coefficients ruled these possibilities out. Nonetheless, similar values for both I=3 and 4 as seen in Table 5–3 made it difficult to firmly assign a spin to the high spin state. Equally helping us discount the I >4 spin assignments are the gamma decay spectroscopy measurements of ^{98}Rb into ^{98}Sr [35] due to strong beta feeding into the K=3 level in Sr. The reason the fitting routine was unable to predict a better spin assignment is the overlapping peaks in the spectrum, which make individual hyperfine transitions difficult to discern. Having identified I=3 and 4 as possible spin assignments based on χ_r^2 values, we have tentatively assigned the high spin state as I=3 as it possesses favourable positive parity, although I=4 spin assignment cannot be discounted as the 2^+ level in Sr could be fed by low spin states of I=1 and the difference in associated χ_r^2 are inconclusive.

To extract changes in mean-square charge radius of a nucleus from the isotope shifts using equation 2.24, the atomic factors, the mass-shift factor $K_{MS}=+200.5(37.7)$ GHz.amu. This was extracted from the latest muonic data. The field shift factor $F_{el}=-567.45(5.70)$ MHz/ $f m^2$ was used from reference [36]. The low spin state in ^{98}Rb has $\delta\langle r_{ch}^2 \rangle^{87,98LS} = 2.063(9)[93](f m^2)$. The high spin state in ^{98}Rb has $\delta\langle r_{ch}^2 \rangle^{87,98HS} = 2.084(9)[93](f m^2)$. The moments were calculated relative to the

known stable isotope ^{87}Rb and calculated to be $\mu = 1.785(1) \mu N$ and $Q_s = 1.431(32)$ b.

The behaviour of the change in the mean-square charge radius of the observed two states in ^{98}Rb are shown along with the previously measured isotopes in Figure 5–8 . The mean square charge radii for the two identified states in ^{98}Rb at $N=61$ are measured to have similar mean-square deformation as at $N=60$ and show no definitive signs of shape coexistence in this region, which was in contrast with what was postulated by Möller [23].

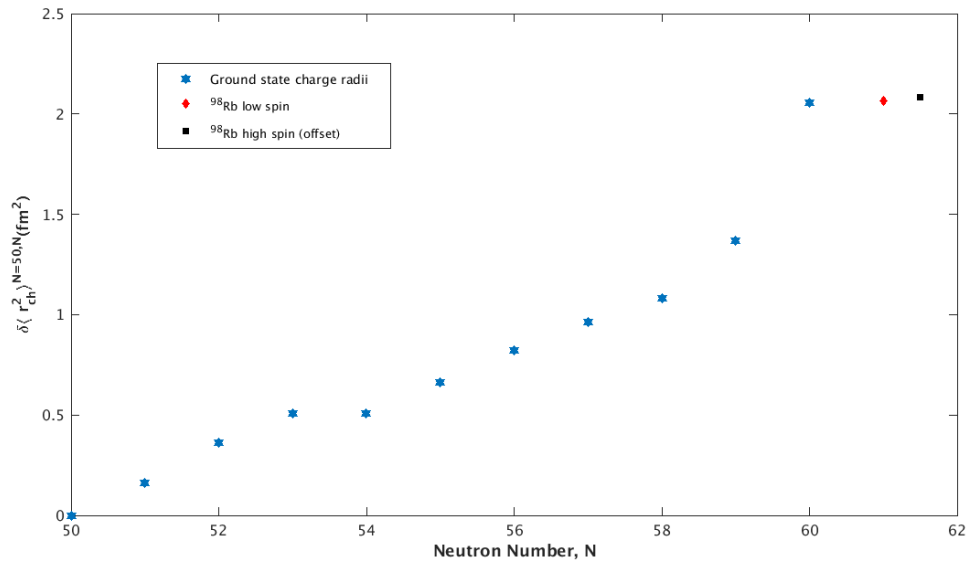


Figure 5–8: The mean square charge radius along the rubidium isotopes between $N=50$ and $N=61$. The value of the isomeric state of ^{98}Rb was shifted by $N=0.5$ to clarify the behaviour at $N=61$.

5.4.5 Spin analysis of ^{99}Rb

Using UC_X targets provides sufficient yields for the collinear laser spectroscopy experiment that allows us to investigate ^{99}Rb . The spin investigation started with testing the different possible spins $I = 3/2, 5/2,$ and $7/2$. We made use of the measured stable isotopes ^{85}Rb with known spin $I=5/2$ and ^{87}Rb with known spin $I = 3/2$. The fitted hyperfine structure using the suggested unmeasured nuclear spin $I = 5/2$ in Thibault et al. [25] is shown in Figure 5–9. The hyperfine coefficients of the fitted spectrum are shown in Table 5–4. The isotope shift is calculated to be $\delta\nu_{IS}^{92,99} = -467(10)$ MHz.

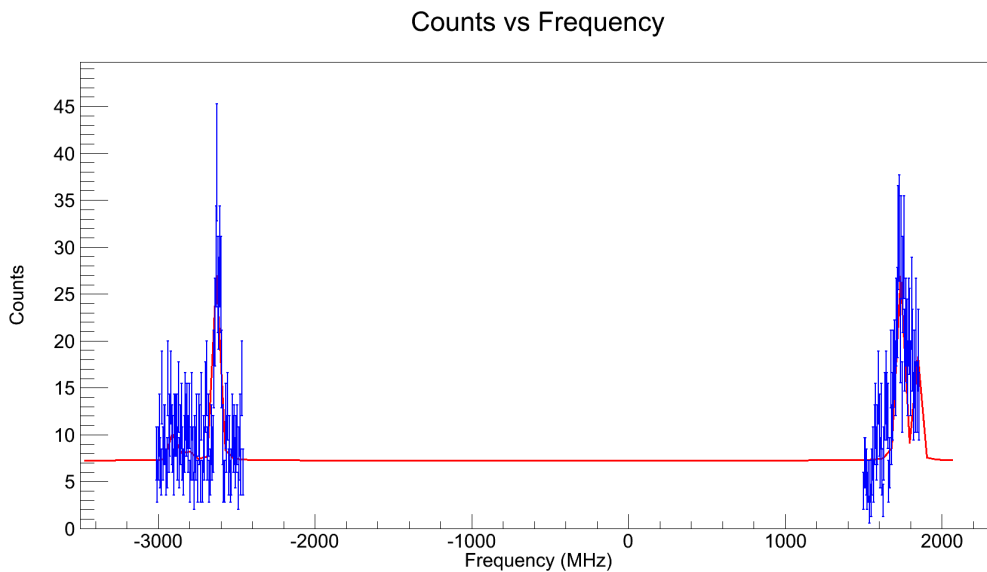


Figure 5–9: The fitted hyperfine structure of ^{99}Rb using $I = 5/2$.

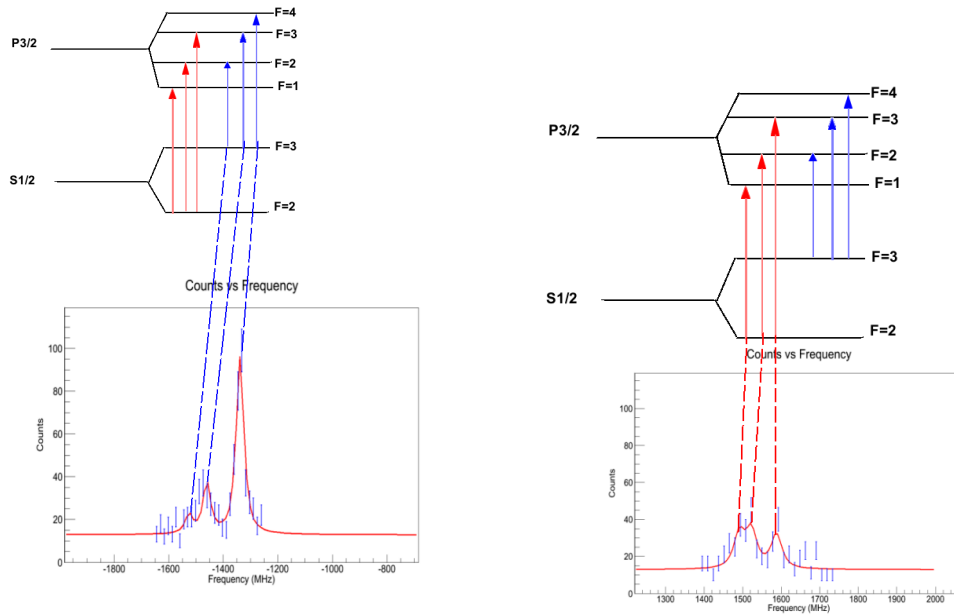
The possible spins for ^{99}Rb can take the values $I = 1/2, 3/2, 5/2, 7/2, \dots$. The D2 transition has an initial state with $J = 1/2$ and a final state $J = 3/2$, so $I = 1/2$ is not a possibility according to section 2.1.1. This would give 2 peaks on the left side

and only one peak on the right. It can be seen from Figure 5–9 that the measured structure has more than one peak on the right side. The other possible nuclear spins were tested using the same fitting routine. The results of the comparison between the considered possible spins are shown in Table 5–4. χ_r^2 and the A hyperfine coefficients are represented as used to either accept or reject the results. The isotope shift of ^{99}Rb while considering spin $I = 5/2$ will be $\delta\nu_{IS}^{92,99} = -467.1(10.3)$ MHz, and $\delta\nu_{IS}^{92,99} = -657.1(10.3)$ for $I = 3/2$.

Table 5–4: The possible spins $I = 3/2, 5/2,$ and $7/2$ hyperfine coefficients, A ratios, and χ_r^2 for ^{99}Rb

| I | A($5s^2S_{1/2}$)(MHz) | A($5p^2P_{3/2}$)(MHz) | B($5p^2P_{3/2}$)(MHz) | A_L/A_U | χ_r^2 |
|-----|-------------------------|-------------------------|-------------------------|-----------|------------|
| 3/2 | 2320.0(1.7) | 59.0(0.2) | 75.0(0.6) | 39.3(0.1) | 1.9 |
| 5/2 | 1555.0(0.7) | 39.0(0.7) | 128.0(1.9) | 39.9(0.7) | 1.8 |
| 7/2 | 1165.0(0.4) | 29.0(0.3) | 155.0(2.8) | 40.2(0.5) | 2.3 |

From the fitting results, the χ_r^2 could allow us to exclude spin $I = 7/2$. Further investigation using two procedures were undertaken :(i) for the suggested nuclear spin $I = 5/2$, the stable isotope ^{85}Rb was used as it has a known nuclear spin $I = 5/2$ [37] as well as for $I = 3/2$, the stable isotope ^{87}Rb was used. An example for the investigated transitions in ^{99}Rb is shown in Figure 5–10. The intensities of the transitions were calculated theoretically using Equation 2.14. Adding to it the real intensities of ^{85}Rb and ^{87}Rb . Both relative intensities were compared to the ^{99}Rb measured relative intensities. The second path (ii) was to deeply investigate the ^{99}Rb intensities and try to exclude any laser pumping effects.



(a) The fitted hyperfine spectrum - high spin frequency of ^{85}Rb with its corresponding transitions

(b) The fitted hyperfine spectrum - low spin frequency of ^{85}Rb with its corresponding transitions

Figure 5-10: Illustration of the hyperfine structure of ^{85}Rb with the corresponding hyperfine transitions.

The normalised relative intensities of the measured stable isotopes along with the theoretical comparison results are comparable to the ^{99}Rb are shown in Table 5-5. The results shows that the experimental data was close to the calculated values from equation 2.14 for both cases. The relative intensities of ^{99}Rb were still not allocated to either spin. The fitted measured spectrum of ^{99}Rb that was shown earlier is fitted with $I = 5/2$ and the results are equally in conclusive as the χ_r^2 method.

Table 5–5: The possible transitions in ^{85}Rb considering spin $I = 5/2$, the measured relative intensities, and the theoretical intensities for both isotopes.

| ^{85}Rb | | | ^{87}Rb | | | ^{99}Rb |
|-------------------|-------------|--------------|-------------------|-------------|--------------|------------------|
| Transition | Theoretical | Experimental | Transition | Theoretical | Experimental | |
| $3 \rightarrow 4$ | 106.9 | 47.5(4.7) | $2 \rightarrow 3$ | 31.5 | 18.0(0.5) | 32 |
| $3 \rightarrow 3$ | 20.5 | 9.1(2.3) | $2 \rightarrow 2$ | 6.4 | 2.0(0.5) | 24 |
| $3 \rightarrow 2$ | 5.8 | 4.3(1.7) | $2 \rightarrow 1$ | 1.3 | 2.0(0.9) | 22 |
| $2 \rightarrow 3$ | 11.7 | 8.4(2.2) | $1 \rightarrow 2$ | 6.0 | 2.0(0.3) | 30 |
| $2 \rightarrow 2$ | 14.4 | 14.8(3.4) | $1 \rightarrow 1$ | 1.2 | 6.00(0.04) | 18 |
| $2 \rightarrow 1$ | 11.4 | 9.9(3.12) | $1 \rightarrow 0$ | 2.4 | 2.0(0.3) | 15 |

A one photon excitation principle was undertaken. It is a process whereby one photon excites an atom, ion, or molecule from a lower energy level to a higher energy level. Another factor was calculating the pumping fraction effect, given by

$$PumpingFraction = Intensity \frac{(2J' + 1)}{(2F' + 1)(2J + 1)}. \quad (5.4)$$

This was used to calculate the modified intensities given by Equation 5.4.5, for a better comparison of the measured intensities of ^{99}Rb .

$$ModifiedIntensity = Intensity * PumpingFraction * npump \quad (5.5)$$

The measured intensities of ^{99}Rb with $I = 5/2$ was investigated and the results for a case similar to the possible transition shown in Figure 5–10 for a nuclear spin $I = 5/2$ are given in Table 5–6.

Table 5–6: *The possible transitions in ^{99}Rb considering spin $I = 5/2$, the measured relative intensities, modified intensities with hyperfine pumping factor.*

| Transition | Theoretical Value with PF | Experimental Value |
|-------------------|---------------------------|--------------------|
| $3 \rightarrow 4$ | 72.0 | 32.0 |
| $3 \rightarrow 3$ | 23.3 | 24.0 |
| $3 \rightarrow 2$ | 4.8 | 22.0 |
| $2 \rightarrow 3$ | 21.0 | 30.0 |
| $2 \rightarrow 2$ | 17.5 | 18.0 |
| $2 \rightarrow 1$ | 11.3 | 15.0 |

Beyond the direct comparison for the intensities of both isotopes ^{85}Rb and ^{99}Rb . The relative intensities show slight effects from pumping effects on the measured intensities during this experiments. The pumping effects were mostly noticed on the cycling transition of the low and high spin frequency transitions. The spin of ^{99}Rb is still uncertain and we conclude that either of the postulated spins are possible at this stage. Future work with a modulated laser beam with the reduction in the hyperfine pumping is the key for an accurate relative intensities.

5.5 Conclusions

The neutron-rich rubidium isotope chain up to $N=61$ is investigated. Specifically, the neutron-rich ^{98}Rb isotope has been studied for the investigation of shape coexistence. Two long-lived nuclear states in ^{98}Rb have been clearly observed for the

first time: a low-spin state, assigned a spin of $I = 0$, and a high-spin state. The high-spin state is tentatively assigned a spin of $I = 3$ based on this work in combination with gamma decay results. The mean-square deformation at $N=61$ shows no definitive signs of shape coexistence in this region as postulated earlier by Möller et al. The hyperfine structure of the neutron-rich ^{99}Rb was observed. Both suggested spins $I = 5/2$ and $I = 3/2$ were based on both experimental results of the stable isotopes ^{85}Rb and ^{87}Rb . Neither spin can be ruled out.

CHAPTER 6

Laser spectroscopy of gallium isotopes

Previous laser spectroscopic studies of neutron-rich gallium isotopes have been carried out at CERN with measurements from $A=80$ to $A=72$ [38], and toward the neutron deficient side from $A=82$ to $A=63$ in [39], excluding ^{65}Ga and ^{67}Ga . This study will extend that work with a goal of reaching ^{62}Ga . In this experiment the hyperfine structure and isotope shifts of $^{63-69}\text{Ga}$ were measured on the, $^2P_{3/2} \rightarrow ^2S_{1/2}$ transition at 417 nm. In addition the shifts and structures of three isotopes $^{66,68,69}\text{Ga}$ were measured on a second transition $^2P_{1/2} \rightarrow ^2S_{1/2}$ at 403 nm. We present the first measurements of the isotope shifts and hyperfine coefficients of ^{65}Ga and ^{67}Ga , and deduce the changes in mean-squared charge radii and nuclear moments. This chapter will include the previously performed measurements at CERN. The hyperfine structures of the neutron-deficient isotopes will be discussed, and the isotope shifts of the entire gallium isotope chain will be presented. By measuring the two transition lines 417 nm and 403 nm of gallium isotopes enable us to study the change in charge radii in two transitions in order to test the atomic theory.

6.1 Introduction

Different gallium campaigns have started an investigation on gallium isotopes toward the neutron-deficient isotopes. This includes the work done by L epine-Szily et al. In [40] starting the attention while measuring the mean-square matter radii of the Ga, Ge, As, Se and Br isotopes from the reaction cross-sections of the fragmented

accelerated krypton beam on thick nickel foil. Gallium isotopes like the others that were investigated, show a noticeable increase in the measured matter radii with decreasing neutron number. A summary of the measurements is shown in Figure 6–1 (taken from [40]).

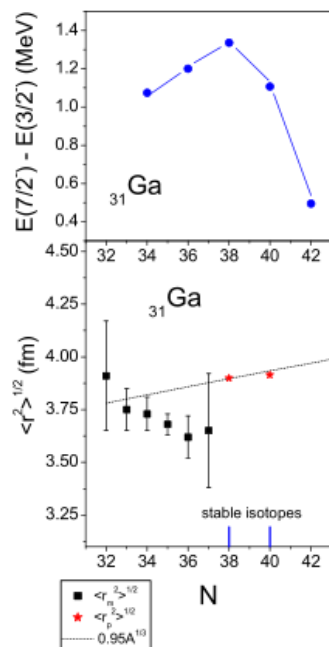


Figure 6–1: The root-mean-square matter radii [bottom] and first excited state energies [top] of the gallium isotopes as a function of neutron number. Figure taken from [40].

To study the deformation of the nucleus, Lépine-Szily et al. investigated the $I = I_{gs} + 2$ state energies, shown in the top plot in Figure 6–1. The effect related to the deformation of the nucleus states that the higher the excitation energy of the 2^+ state or $I = I_{gs} + 2$ state, the less deformed is the nucleus [41]. Around $N = 37, 38$ the gallium isotopic chain present a maximum in excitation energy and thus a minimum in deformation, which is correlated with a minimum in the matter radii.

For lower N values the excitation energies very slightly decrease. The deformation parameter β of the neighbouring even-even germanium and zinc isotopes between $N = 40$ down to $N = 30$ were used to study this increase in the matter radius by the observation of any possible deformations [42]. The results is shown in Figure 6–2. The result suggests that below $N=38$ very little change in deformation occurs.

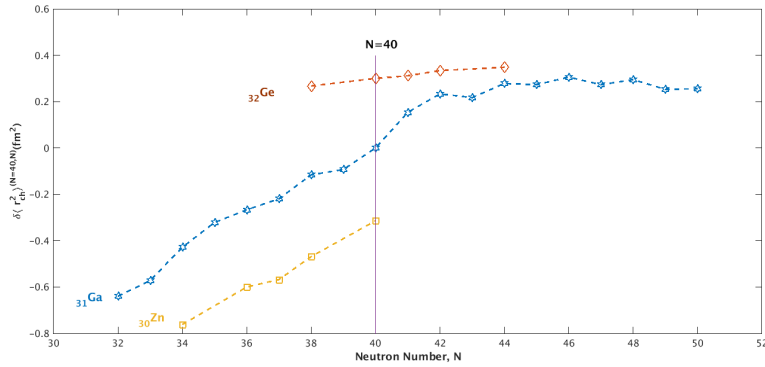


Figure 6–2: Plot of the deformation parameter β against neutron number in zinc [diamond] and germanium [square].

Since it was not clear that there was an obvious increase in deformation, Lépine-Szily et al. postulated that the effect could be produced by the development of a proton skin. As neutrons are removed from the nucleus the repulsive force of the protons could act to push them further apart and actually increase the matter radius of the nucleus. Therefore a study of both the change in mean-squared charge radius of $^{63-71}\text{Ga}$, together with quadrupole moment measurements should show whether or not a deformation change is occurring.

6.2 Experimental setup

For this experiment, a zirconium carbide target (ZrC) was used to produce neutron-deficient gallium isotopes. This target provides very clean Ga beams, with no TiO contamination. In addition, TRIUMF's Resonance Ionisation Laser Ion Source(TRILIS) was used to selectively ionize atoms. 40 μA of 480 MeV p^+ ions impinged on a ZrC target. Radioactive Ga^+ ions were extracted at 30 keV. Table 6–1 shows the half-lives and the yields of the isotopes studied.

Table 6–1: Summary of half-lives and yields of Ga isotopes from ZrC target. The yields are given in units of ions/s. Note: the yield of ^{67}Ga was not directly measured due to its long half-life.

| A | $T_{1/2}$ | Yield(ISAC) |
|----|-----------|----------------------|
| 62 | 116.18 ms | 3×10^3 |
| 63 | 32.4 s | 2×10^6 |
| 64 | 2.627 min | 2.9×10^7 |
| 65 | 15.2 min | 2.5×10^8 |
| 66 | 9.49 h | 1×10^9 |
| 67 | 3.26 d | See caption |
| 68 | 67.62 m | 1×10^9 |
| 69 | stable | 2.5×10^{14} |

The low-lying atomic states in gallium are shown in Figure 6–3. The two possible atomic transitions in gallium that were used to measure the hyperfine structure are: (i) $^2P_{1/2} \rightarrow ^2S_{1/2}$ (403 nm) transition and (ii) $^2P_{3/2} \rightarrow ^2S_{1/2}$ (417 nm) transition. The natural linewidth of both transitions is 25 MHz. The 417 nm transition was

used to measure the IS and extract the different nuclear properties such as nuclear moments and mean square charge radii. This transition is the only possible one that can access quadrupole moments. Several measurements were made on the 403 nm line for $^{66,68,69}\text{Ga}$ isotopes which were used in combination with the measurements on the 417 nm transitions to check whether charge radii are identical across different transitions .

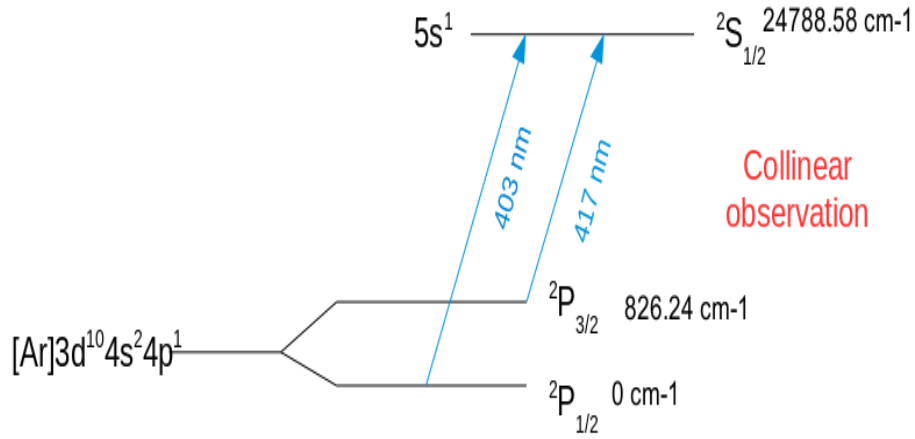


Figure 6–3: The atomic transitions chosen in gallium for this experiment [43]

The continuous beam from ISAC was bunched using TITAN’s RFQ, then neutralised by passing through the charge exchange cell (CEC), containing rubidium vapour at $\approx 200^{\circ}\text{C}$. The neutralisation efficiency was measured to be 30%. The Ga ion beam was then accelerated by applying an additional acceleration potential to the CEC to allow the atom to be scanned via the Doppler shift. The Ti:Sa laser was frequency-doubled using a wave-train frequency doubler as described in section 4.3 to produce light of 417, 403 nm. The light was transported via optical fibres . This delivered up to ≈ 7 mW to the beamline.

6.3 Data analysis

During the experiment, several scans were performed for each isotope, and were then individually analysed. Predictions of both the hyperfine peak energies and isotope shift were undertaken to assist the experiment. Isotope shifts of the isotopes measured for the first time were extrapolated from the known IS in [30]. The hyperfine coefficients were also extrapolated from the A_L/A_U ratio of the previously measured gallium isotopes with $A_L/A_U = 5.592 \pm 0.002$. A scan for ^{69}Ga as a reference stable isotope scan was made in between every change of mass in the separator to detect any drifts in the centroids of the transitions due to drifts in the laser frequency. As described in section 3.4 a histogram of counts vs. frequency was created from the data. For each scan, a data file of photon counts against the laser frequency was produced and used for the analysis. The analysis of the gallium data was performed using a χ^2 minimisation technique. A fitting code in Root was used to fit the spectra. A simulated hyperfine structure was made using predicted energy shifts with a fixed nuclear spin. The line shapes were simulated using Voigt profiles. The fitting parameters were the centroid for each transition, the background counts, and the full-width at half maximum (FWHM) was kept constant across all transitions in a single scan. The Lorentzian/Gaussian ratio, the intensities of the transitions and the hyperfine parameters, $A(P_{3/2}), A(S_{1/2}), B(P_{3/2}), A(P_{3/2})$ were constrained to $A(P_{1/2})$ by a fixed known ratio among the Ga isotopes to be +5.592 to assist the fitting. The measured hyperfine structure of the gallium isotopes in the two lines (417 nm) and (403 nm) transitions are shown in Figures 6–4 and 6–5.

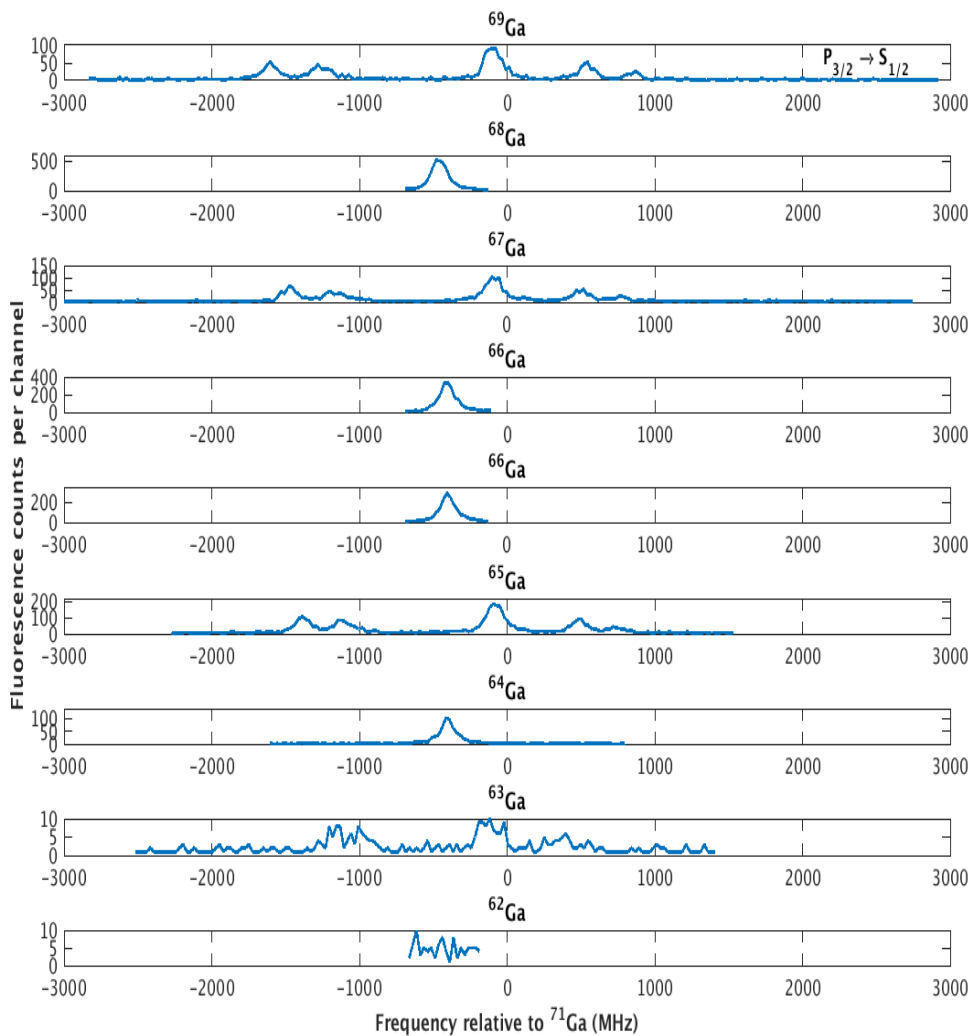


Figure 6-4: The measured hyperfine structure of all gallium isotopes in the $^2P_{3/2} \rightarrow ^2S_{1/2}$ (417 nm) transition. The frequencies shown are relative to ^{71}Ga centroid (MHz).

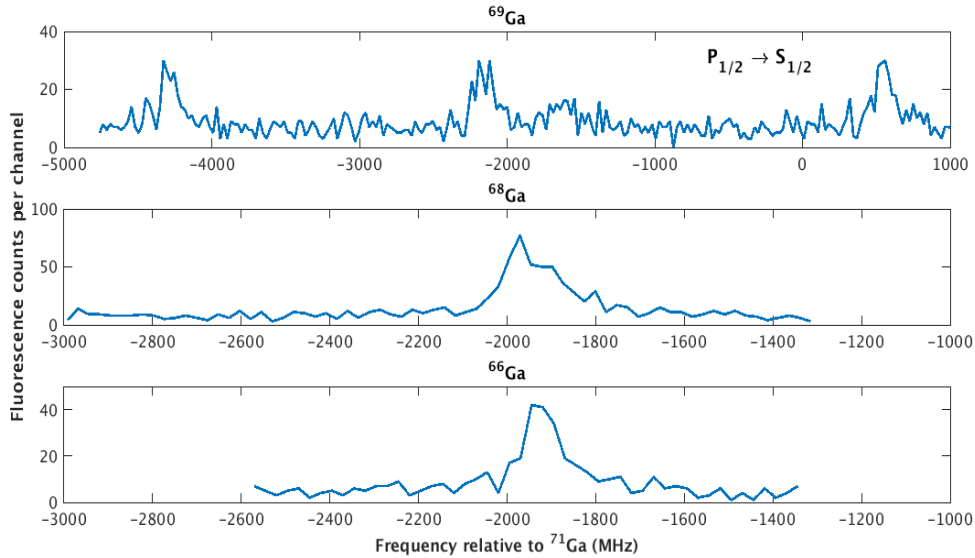


Figure 6–5: The measured hyperfine structure of $^{66,68,69}\text{Ga}$ isotopes in the $^2P_{1/2} \rightarrow ^2S_{1/2}$ (403 nm) transition. The frequencies shown are relative to ^{71}Ga centroid (MHz).

6.3.1 Laser spectroscopy of ^{69}Ga

In order to be able to measure isotope shifts and to extract the changes in the RMS charge radii a reference isotope is required. For this work ^{69}Ga was chosen since it is one of the stable gallium isotopes with known spin, hyperfine structure and moments. The results shown in Table 6–2 were taken from the run shown in Figure 6–6 which was used as a reference for the other isotopes in the sequence.

Table 6–2: Hyperfine coefficient values of ^{69}Ga

| A | Source | I | $A(S_{1/2})$ (MHz) | $A(P_{3/2})$ (MHz) | $B(P_{3/2})$ (MHz) | $\delta\nu_{IS}^{69,A}$ |
|----|-----------|-----|-----------------------|-----------------------|-----------------------|-------------------------|
| 69 | This work | 3/2 | 1070.7(1.0) | 191.5(0.3) | 62(2) | 0 |
| | Ref[39] | 3/2 | 1069.7(1.5) | 191.5(9) | 63(2) | 0 |

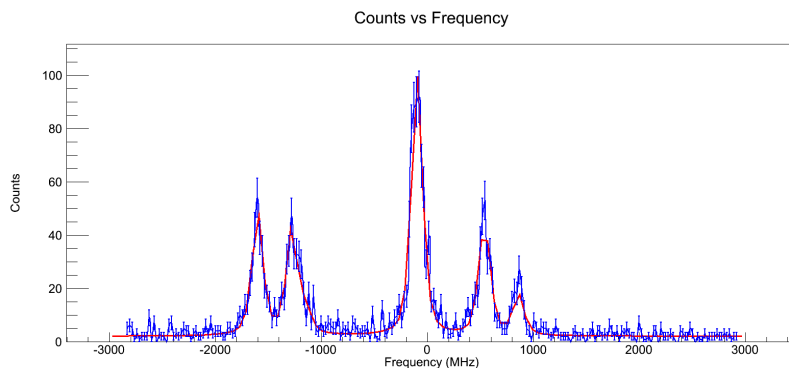


Figure 6–6: The fitted hyperfine structure [solid red line] of ^{69}Ga , the stable reference isotope.

In Figure 6–6 the fitted structure of the stable isotope ^{69}Ga is shown. The isotope shift $\delta_{IS}^{71,69}$ for the $P_{3/2} \rightarrow S_{1/2}$ transition is 39.6(3.5) MHz. The isotope shift $\delta_{IS}^{71,69}$ for the $P_{1/2} \rightarrow S_{1/2}$ transition is 32.8(3.5) MHz [44].

The hyperfine structure of ^{69}Ga has been previously observed [38, 39]. From Table6–2 the measured hyperfine coefficients are in agreement with literature.

6.3.2 Laser spectroscopy of ^{68}Ga

The ground-state spin of ^{68}Ga is already known to be $I = 1$ and the magnetic dipole and electric quadrupole moments have been measured as $+0.01175(5) \mu_N$ and $+0.0277(14) \text{ b}$ respectively using the atomic beam magnetic resonance technique

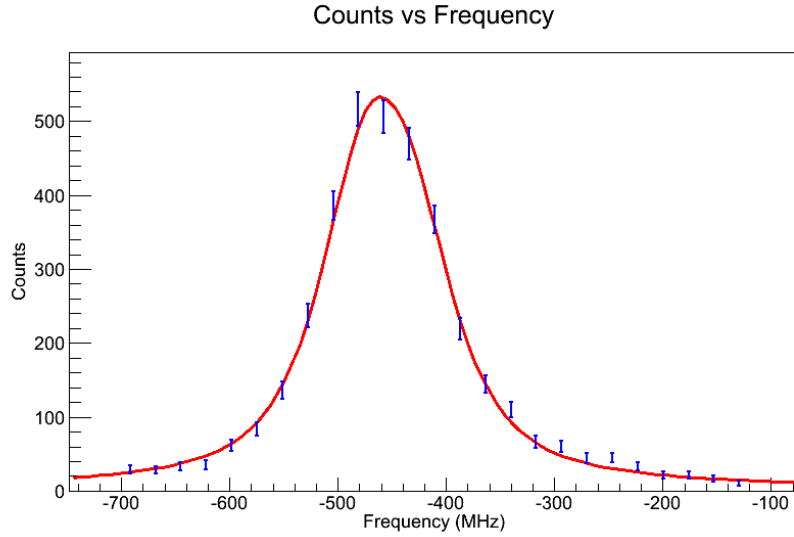


Figure 6–7: The fitted hyperfine structure [solid red line] of ^{68}Ga . The individual predicted transitions are not shown.

[26]. From these measurements, the hyperfine coefficient values for the atomic transition for ^{68}Ga can be calculated and used to predict its hyperfine structure. The coefficients were calculated with respect to hyperfine coefficients and moments of ^{69}Ga as reference values [26]. The expected hyperfine coefficient values of ^{68}Ga were determined to be:

Table 6–3: Hyperfine coefficient values of ^{68}Ga

| A | Source | I | $A(S_{1/2})$ (MHz) | $A(P_{3/2})$ (MHz) | $B(P_{3/2})$ (MHz) | $\delta\nu_{IS}^{69,A}$ |
|----|-----------|---|-----------------------|-----------------------|-----------------------|-------------------------|
| 68 | This work | 1 | 9.7(10.7) | 1.6(4) | 10.5(6.9) | 4.1(2.6) |

These coefficients are very small and will create extremely small energy shifts in the hyperfine structure, as seen in Table 6–3.

The hyperfine structure was not resolved, consistent with the results from previous work [39]. Since the splittings are so small the individual transitions could be moved around relative to each other within the error allowed by the fitting routine. From the analysis of the hyperfine structure of ^{68}Ga the hyperfine coefficients of ^{68}Ga were not extracted with more precision than the previously known values and the accuracy of the fitting routine showed no signs that they are any different from the literature values [39].

6.3.3 IS and mean charge radii of ^{67}Ga

As mentioned earlier, prior this experiment the charge radii of ^{67}Ga was not known. The ground state spin is already known to be $I = 3/2$ [45]. This experiment is the first measurement for the charge radii of ^{67}Ga , where the hyperfine structure was measured and the fitting hyperfine coefficients were used to calculate the charge radii. The isotope shift to ^{69}Ga and extracted hyperfine coefficient values of ^{67}Ga are given in Table 6–4:

Table 6–4: Hyperfine coefficient values of ^{67}Ga

| A | Source | I | A($S_{1/2}$) (MHz) | A($P_{3/2}$) (MHz) | B($P_{3/2}$) (MHz) | $\delta\nu_{IS}^{69,A}$ |
|----|-----------|-----|-------------------------|-------------------------|-------------------------|-------------------------|
| 67 | This work | 3/2 | 981.4(3.1) | 172.2(1.5) | 73.1(3.6) | +30.3(3.4) |
| 67 | Ref [38] | 3/2 | 979.7(2.5) | 175.8(1.0) | 73(4) | |

6.3.4 IS and mean charge radii of ^{65}Ga

Prior to this experiment, the charge radii of ^{65}Ga and ^{67}Ga were not known, due to TiO contamination problems during the latest Ga experiment at CERN.

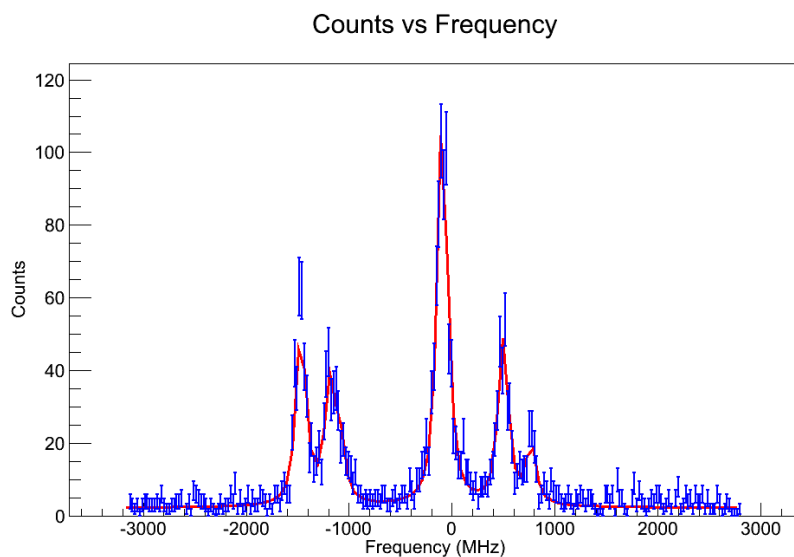


Figure 6–8: The fitted hyperfine structure [solid red line] of ^{67}Ga .

The ground-state spin is already known to be $I = 3/2$ for both isotopes as well as the hyperfine coefficients. From the current experimental measurements, five peaks were resolved, while the sixth transition peak (six possible hyperfine transitions between the lower and the upper states) appears within the peak that consist of two overlapping peaks. However, the resolution was sufficient to resolve and extract the hyperfine coefficients, IS and charge radii. Figure 6–9 shows the measured spectrum for ^{65}Ga .

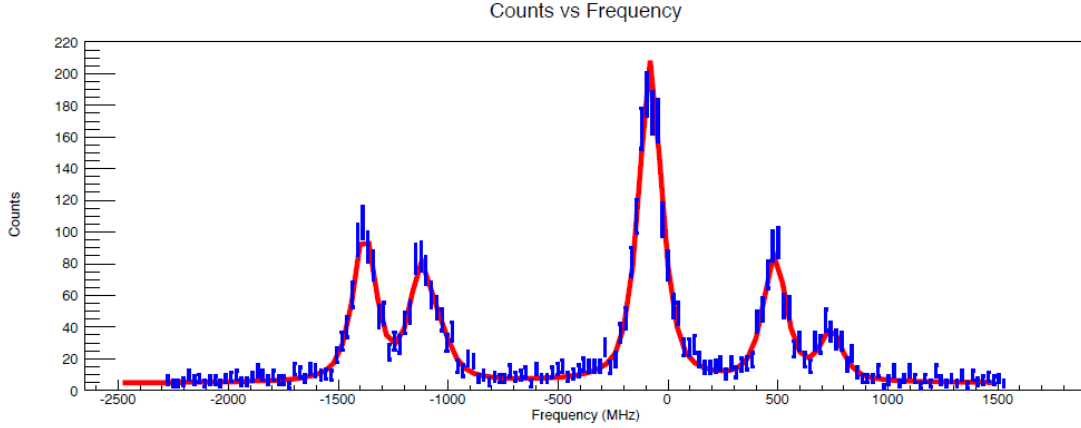


Figure 6–9: The fitted hyperfine structure [solid red line] of ^{65}Ga . The plot shows the number of photon counts vs. frequency of the atomic transition.

The hyperfine structure was fitted using the same fitting routine that was mentioned previously, where the possible hyperfine coefficients combinations were restricted to the A ratio constraint while minimising the χ_r^2 value that provides the best fit. The results of ^{65}Ga measurements are shown in Table 6–5

Table 6–5: Hyperfine coefficient values of ^{65}Ga

| A | Source | I | $A(S_{1/2})$ (MHz) | $A(P_{3/2})$ (MHz) | $B(P_{3/2})$ (MHz) | $\delta\nu_{IS}^{69,A}$ |
|----|-----------|-----|-----------------------|-----------------------|-----------------------|-------------------------|
| 65 | This work | 3/2 | 932.82(2.21) | 164.44(1.17) | 72.16(3.57) | +66.05(3.42) |

6.3.5 Measurements of ^{64}Ga and ^{66}Ga

^{64}Ga and ^{66}Ga have known ground state spins $I = 0$ from $\beta - \gamma$ correlation and atomic beam magnetic resonance experiments [46]. In the case of $I=0$ there is no hyperfine splitting of the atomic state energies, and a single peak was observed for

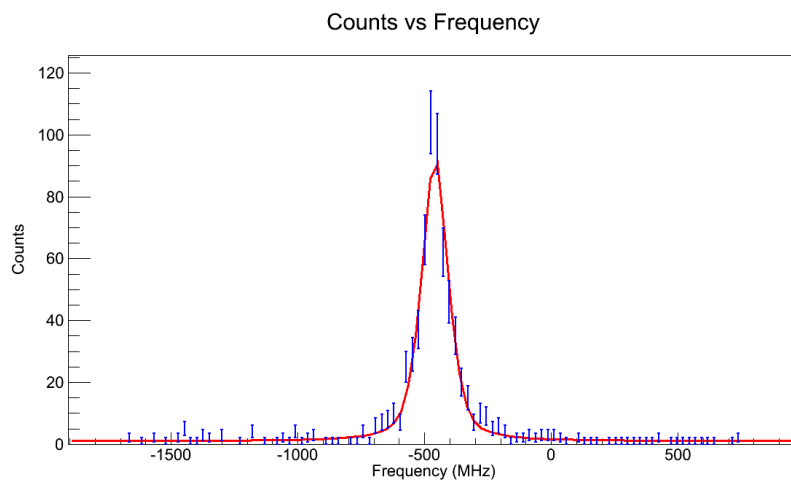


Figure 6–10: The fitted hyperfine structure [solid red line] of ^{64}Ga with a single peak ($I=0$).

Table 6–6: Isotope shifts from ^{69}Ga .

| A | $\delta_{IS}^{69,A}$ (MHz) |
|----|----------------------------|
| 64 | 53.81(3.58) |
| 66 | 53.73(3.26) |

each isotope as expected. Isotope shifts were obtained from the different scans that were performed. The assigned spin was tested. The measured structures of ^{64}Ga and ^{66}Ga with the fitted structure are shown in 6–10 and 6–11 respectively.

We used the same fitting routine with $I=0$ for the ground state spin. The fitted structure shows an agreement with the assigned spin value. The FWHM was around 100 MHz, which excludes any suggestions of other hidden overlapped structure. The isotope shifts from ^{69}Ga were extracted and the results are shown in Table 6–6.

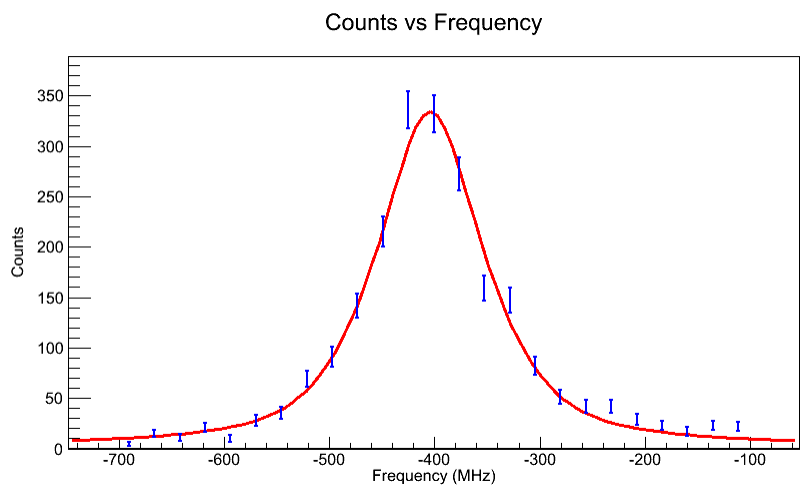


Figure 6–11: The fitted hyperfine structure [solid red line] of ^{66}Ga with a single peak ($I=0$).

6.3.6 Measurements of ^{63}Ga

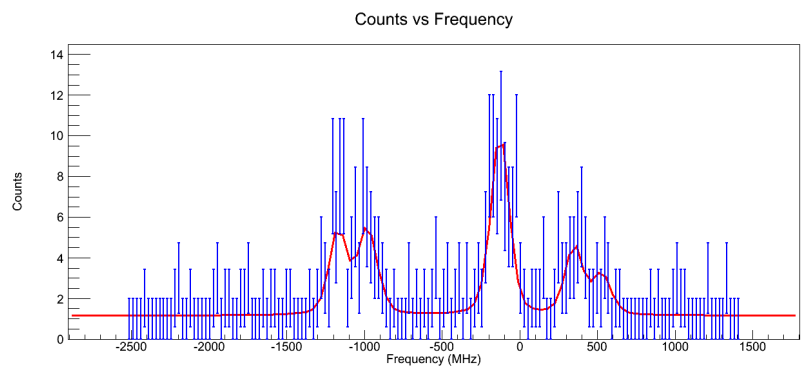


Figure 6–12: The fitted hyperfine structure [solid red line] of ^{63}Ga .

The hyperfine structure was fitted using the same fitting routine that was mentioned previously. Due to the low statistics the ratio of A_{upper}/A_{lower} was kept fixed, and the possible hyperfine coefficients combinations were restricted to the A ratio

constraint while minimising the χ_r^2 value that provide the best fit. The results of ^{63}Ga measurements are shown in Table 6–7.

Table 6–7: *Hyperfine coefficient values of ^{63}Ga .*

| A | Source | I | A($S_{1/2}$) (MHz) | A($P_{3/2}$) (MHz) | B($P_{3/2}$) (MHz) | $\delta\nu_{IS}^{69,A}$ |
|----|-----------|-----|-------------------------|-------------------------|-------------------------|-------------------------|
| 63 | This work | 3/2 | 759.4(15) | 131.4(6) | 83.1(17) | 78.6(10) |
| 63 | Ref[39] | 3/2 | 778.9(22) | 139.3(4) | 77.5(28) | 81(6) |

From Table 6–7 the measured hyperfine coefficients are in agreement with literature [39],

6.3.7 Measurements of ^{62}Ga

A number of scans were made in the frequency region where a single peak for ^{62}Ga (I=0) was expected. However, the yield of ^{62}Ga ions was just ≈ 1000 ions/s, an order of magnitude lower than that require for satisfactory statistics. It is hoped that a future run will permit successful measurements on this isotope. From the measured gallium isotopes of $^{63-69}\text{Ga}$ and the extracted nuclear properties which agree with literature, therefore, there is high confidence for future measurement of ^{62}Ga .

6.3.8 Nuclear moment analysis

Following the measurements of the hyperfine coefficients of ^{63}Ga , ^{65}Ga and ^{67}Ga their magnetic dipole and electric quadrupole moments can be determined. The hyperfine coefficients and moments of the reference isotope, ^{69}Ga used, were measured as described earlier in Chapter 2. The extracted $A(5s2S_{1/2})$ and $B(4p2P_{3/2})$ hyperfine coefficient values from Tables 6–7, 6–5 and 6–4 were used. The new moment values

were deduced using, $\mu = \frac{AI\mu_{ref}}{A_{ref}I_{ref}}$ and $Q_s = \frac{BQ_{sref}}{B_{ref}}$. For the reference isotopes the values from [26] were used.

Using these values, the magnetic moments of ^{63}Ga , ^{65}Ga and ^{67}Ga were extracted and presenting in Table 6–8.

Table 6–8: Nuclear moments of $^{63,65,67}\text{Ga}$.

| A | $\mu(\mu_N)$ | $Q_s(\text{b})$ |
|----|--------------|-----------------|
| 63 | 1.464(4) | 0.226(14) |
| 65 | 1.758(5) | 0.204(13) |
| 67 | 1.849(5) | 0.207(13) |

As can be seen from the results, the magnetic moment increases with A, while the quadrupole moment which is considered to be a measure for the nuclei deformation is decreasing.

6.3.9 Changes in charge radii from two transitions

During the gallium experiment, the laser spectroscopy group was able to measure ^{66}Ga , ^{68}Ga and ^{69}Ga in two transitions lines (403 nm and 417 nm). The isotope shifts for each isotope to ^{69}Ga and ^{71}Ga in the two transition lines are shown in Table 6–9.

Table 6–9: *Isotope shifts from ^{69}Ga in the 417 nm and the 403 nm transition lines*

| A | $\delta_{IS}^{69,A}$ | $\delta_{IS}^{69,A}$ |
|----|----------------------|----------------------|
| | 417 nm | 403 nm |
| 66 | 53.73 (3.2) | -14.96 (7.2) |
| 68 | 4.09 (2.6) | 11.28(7.8) |
| 69 | 0 | 0 |
| 71 | -39.6(3.5) | -32.8(3.5) |

A previous calculations for the atomic factors in [38] using a multiconfigurational Dirac-Fock (MCDF) calculations gave an estimation of $K_{MS}=-431$ GHz amu and $F_{el}=+400$ MHz. fm^{-2} for the mass-shift factor and the field shift factor, respectively. A new un-published source [47] depending on a developed multiconfigurational electronic method was able to provide us with new estimated $K_{MS}=-21$ GHz amu and $F_{el}=+429$ MHz. fm^{-2} .

6.3.10 Extracting the changes in mean-square charge radii

The change in mean-square charge radii can be extracted from the isotope shift with the presence of the atomic factors, the mass-shift factor K_{MS} and the field shift factor F_{el} using equation 6.1:

$$\delta\nu_{IS}^{AA'} = K_{MS} \frac{m_A - m'_A}{m_A m'_A} + F_{el} \langle r_{ch}^2 \rangle^{AA'}. \quad (6.1)$$

Table 6–10: Isotope shifts and changes in mean-square charge radii relative to ^{71}Ga . Statistical errors are shown in parentheses and systematic errors are in square brackets. The $\delta\langle r_{ch}^2 \rangle$ values in column 3 are calculated using our data and the F_{el} and K_{ms} factors used in reference [39]. Those in column 4 are obtained with the F_{el} factor from reference [39] and K_{ms} adjusted to fit the muonic $\delta\langle r_{ch}^2 \rangle$ data for the ^{69}Ga - ^{71}Ga pair. Those in column 5 are obtained with the values for F_{el} and K_{ms} from ref [47]

| A | $\delta_{IS}^{71,A}$ | $\delta\langle r_{ch}^2 \rangle^{71,A}(fm^2)$ | $\delta\langle r_{ch}^2 \rangle^{71,A}(fm^2)$ | $\delta\langle r_{ch}^2 \rangle^{71,A}(fm^2)$ |
|----|------------------------|---|---|---|
| | This Work [†] | Using Ref [39] | | |
| 63 | 118.2(10)[18] | -0.643(14)[140] | -0.640(5)[140] | 0.184(15)[140] |
| 64 | 93.4(5)[15] | -0.579(12)[120] | -0.572(5)[120] | 0.37(20)[120] |
| 65 | 105.7(5)[11] | -0.687(20)[100] | -0.428(5)[100] | 0.1703(20)[100] |
| 66 | 93.3(5)[11] | -0.329(8)[80] | -0.322(5)[80] | 0.170(11)[80] |
| 67 | 69.9(5)[6] | -0.445(20)[50] | -0.267(5)[50] | 0.121(20)[50] |
| 68 | 43.69(4)[4] | -0.214(5)[50] | -0.219(5)[50] | 0.067(20)[50] |
| 69 | 39.6(4)[2] | -0.116(3)[20] | -0.116(5)[20] | 0.0723(10)[20] |

[†] systematic errors were estimated from this work with reference [39] based on the systematic laser drifts.

The charge radii were extracted using two computational methods (i) Reference [47] with $F_{el}=+429$ MHz. fm^{-2} , estimated from computations, and $K_{MS}=-21$ GHz.amu. This source depends on a developed multiconfigurational electronic method was able to provide us with a new estimated values, on the deepest electronic configuration method. (ii) Those in column 4 are obtained with the F_{el} factor from reference [47] and K_{ms} adjusted to fit the muonic $\delta\langle r_{ch}^2 \rangle$ data for the ^{69}Ga - ^{71}Ga pair.

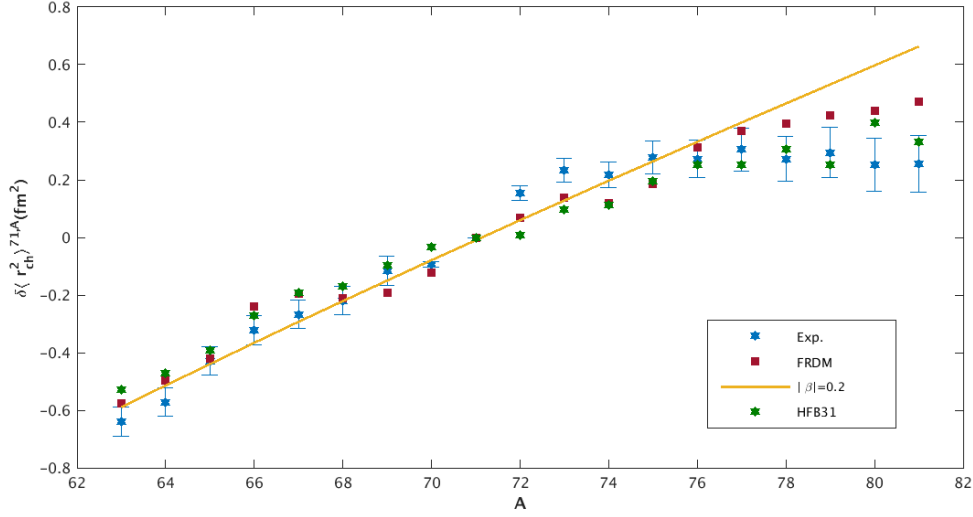


Figure 6–13: Changes in mean-square charge radii of the gallium isotopes, from ^{71}Ga , calculated using different models. The experimental points were calculated using constants from [47]. The FRDM predictions based on the Finite Range Droplet Model. The HFB31 calculations are taken from [48].

Figure 6–13 shows the experimental results of the $\langle \delta r_{ch}^2 \rangle$ for the gallium isotopes between $A=63$ and $A=81$ relative to ^{71}Ga . These values were calculated using the isotope shifts that were measured in this work for $^{63-69}\text{Ga}$, combined with the results from [39] for the isotopes above ^{71}Ga . The atomic factors were taken from [47]. As it can be seen the results were within a good agreement with the predicted values using the Finite Range Droplet Model (FRDM) and the calculations from the Hartree-Fock calculations for $Z=31$ in reference [48]. The deformation parameter $|\beta| = 0.2$ was also taken from [48]. The Hartree-Fock calculations suggested a constant deformation in the neutron-rich isotopes side.

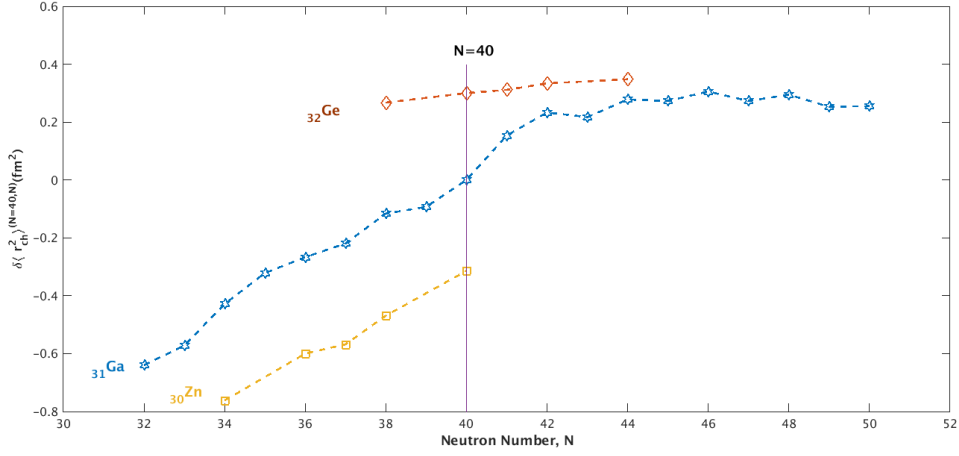


Figure 6–14: The measured changes in mean-squared charge radii of gallium isotopes between the neighbouring even-even germanium and zinc isotopes.

The behaviour of the $\langle \delta r_{ch}^2 \rangle$ of the measured gallium isotopes between the neighbouring even-even germanium and zinc isotopes is shown in Figure 6–14. The Data for the Zn and Ge isotopes are from [49]. No deviation is noticed for the gallium.

6.4 Conclusions

The neutron-deficient gallium isotopes down to $N=32$ have been measured via laser spectroscopy. Their hyperfine structures and isotope shifts are reported in this work. The magnetic dipole and electric quadrupole moments of ${}^{65}\text{Ga}$ and ${}^{67}\text{Ga}$ were measured for the first time, for ${}^{65}\text{Ga}$: $\mu = +1.758(5)\mu_N$ and $Q_s = +0.226(14)b$ respectively. For ${}^{67}\text{Ga}$ the measured moments were $\mu = +1.849(5)\mu_N$ and $Q_s = +0.207(13)b$. Analysis of the trend in the neutron-deficient charge radii illustrate that there is no evidence for deformations from the behaviour in the gallium down to $N = 32$. With regard to the observed ${}^{62}\text{Ga}$, its isotope shift and its charge radius

could not be determined but narrowed down, due to the low yield of this isotope. A motivated discussion for a future investigation on ^{62}Ga is included.

CHAPTER 7

Conclusions and summary

7.1 This work

The neutron-rich rubidium isotope chain up to $N=61$ is investigated. Specifically, the neutron-rich ^{98}Rb isotope has been studied for the investigation of shape coexistence. Two long-lived nuclear states in ^{98}Rb have been clearly observed for the first time: a low-spin state, assigned a spin of $I = 0$, and a high-spin state. The high-spin state is tentatively assigned a spin of $I = 3$ based on this work in combination with gamma decay spectroscopy results. The hyperfine structure of the neutron-rich ^{99}Rb was observed. The suggested assigned spin $I = 5/2$ was studied based on both experimental results of the stable isotopes ^{85}Rb and ^{87}Rb . The spin of ^{99}Rb is still uncertain and we conclude that either of the postulated spins are possible at this stage. Future work with a modulated laser beam with the reduction in the hyperfine pumping is the key for an accurate relative intensities.

The neutron-deficient gallium isotopes down to $N=32$ have been measured via laser spectroscopy. Their hyperfine structures and isotope shifts are reported in this work. The magnetic dipole and electric quadrupole moments of ^{65}Ga and ^{67}Ga were measured for the first time, for ^{65}Ga : $\mu = +1.758(5)\mu_N$ and $Q_s = +0.226(14)b$ respectively. For ^{67}Ga the measured moments were $\mu = +1.849(5)\mu_N$ and $Q_s = +0.207(13)b$. Analysis of the trend in the neutron-deficient charge radii illustrate that there is no evidence for deformations from the behaviour in the gallium in the

$N = 32$ region. With regard to the observed ^{62}Ga , its isotope shift and its charge radius could not be determined but narrowed down. Due to the low yield of this isotope. A motivated discussion for a future investigation on ^{62}Ga is included.

7.2 Motivation for future work

The motivation of this work was measuring the charge radius of ^{62}Ga that can be used to test the errors from the nuclear-structure corrections that is used to test the unitary of the the CKM matrix. In this experiment an approach to measure the charge radius of ^{62}Ga will be discussed although the low statistics due to a low radioactive beam yield than requested caused a high uncertainty of the isotope shift of ^{62}Ga and extracted charge radii.

Part of the Standard Model (SM), the Cabibo-Kobayashi-Maskawa (CKM) matrix describes the mixing of quark flavors [50]. The unitary of the CKM matrix is one of the pillars of the SM. The CKM matrix takes the form

$$\begin{pmatrix} V_{ud} & V_{us} & V_{ub} \\ V_{cd} & V_{cs} & V_{cb} \\ V_{td} & V_{ts} & V_{tb} \end{pmatrix} \quad (7.1)$$

The elements should be measured as accurately and precisely as possible. The sum of the top elements of V_{CKM} provides the most precise test of the unitarity of CKM with $|V_{ud}|^2 + |V_{us}|^2 + |V_{ub}|^2 = 1$. Non-unitary of CKM would require new physics phenomena, such as the existence of right-handed currents, extra Z bosons or another quark generation. The up-down quark mixing matrix element is obtained through the most precise method, via the superallowed ($0^+ \rightarrow 0^+$) Fermi β decays. The corrected

F_t value of the beta transition is defined in the expression,

$$F_t = f_t(1 + \delta'_R)(1 + \delta_{NS} - \delta_C) = \frac{K}{2G_V^2(1 + \Delta_R^V)} \quad (7.2)$$

The uncorrected f_t value is related to the measured half-lives, branching ratios and Q -Value of the β decay. The δ'_R and δ_{NS} are transition-dependent corrections, and δ_C is the isospin symmetry breaking term. The term Δ_R^V is transition-independent and K is a constant that equals $8120.2787(11) \times 10^{-10} GeV^{-4}s$. The G_V is the vector coupling constant of semileptonic weak interactions. The Conserved Vector Current(CVC) hypothesis assumes G_V remains unchanged in this case, V_{ud} can then be obtained from $V_{ud} = \frac{G_V}{G_F}$, where G_F is the weak interaction constant for leptonic muon decay, while G_V is defined in terms of the corrected F_t .

Global evaluations of the value of F_t involve the 13 most precisely measured superallowed β^- emitters which span a wide Z range ($6 \leq Z \leq 37$). Towner and Hardy made the latest evaluation of the F_t [4]. The V_{ud} was evaluated to be 0.97425(22). When it is combined with the values of V_{us} and V_{ub} obtained from Kaon and B decays, the unitary test becomes $|V_{ud}|^2 + |V_{us}|^2 + |V_{ub}|^2 = 0.9999(6)$ [4].

In order to reduce the uncertainty of V_{ud} , the measurements and theoretical corrections must be refined. The latest global evaluation is shown in Figure 7-1. From the figure above, it can be seen that all the data points are consistent with the world average of F_t represented by the grey line with a thickness of $1 \pm \sigma$ to be the error. The results show that the values for ^{62}Ga and ^{74}Rb stands out from the rest of the data set. They also show how the theoretical correction applied to the f_t values

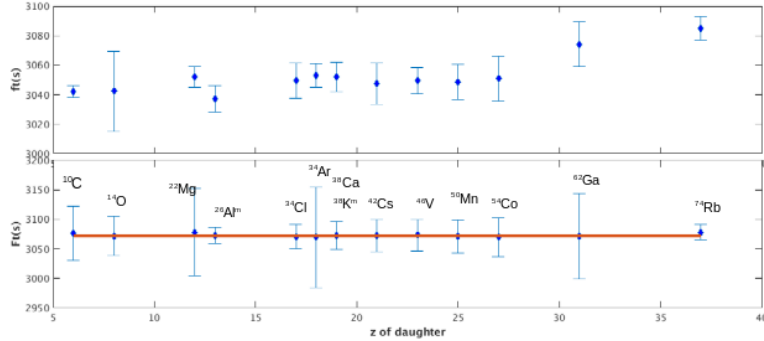


Figure 7–1: The uncorrected f_t and corrected F_t values for the 13 selected superallowed cases. Taken from [4]

inflates the errors of each individual case. The effect on the F_t value of ^{62}Ga is dramatic. The isospin-symmetry-breaking correction δ_C accounts for the radial-mismatch factor between parent and daughter isotopes. Towner and Hardy split δ_C into two contributions $\delta_C = \delta_{C1} + \delta_{C2}$ in their work [4]. δ_{C1} reflects differences in isospin mixing between the parent and the daughter isotopes that can be determined from the shell-model calculation, while the second term δ_{C2} accounts for the radial overlap correction where the ground-state mean square charge radius is used to fix the radius parameter of the Coulomb term in the Saxon-Woods central potential. The value of δ_{C1} is sensitive to the charge dependence of the effective interaction. In the case of ^{74}Rb our collaboration has recently measured the charge radius of ^{74}Rb [16]. The contribution of ^{74}Rb is approximately 10% of δ_{C2} . They computed δ_{C2} of ^{74}Rb based on extrapolations for the mean square charge radius ($\langle r_{ch}^2 \rangle^2 = 4.18(10) \text{ fm}$ [16]. With this measurement, an improvement from $\delta_{C2}^{old} = 1.5(30)$ to $\delta_{C2}^{new} = 1.5(25)$ was achieved, reducing the uncertainty and putting the value of δ_C on solid experimental ground.

The case of ^{62}Ga has been receiving obvious attention recently. Its mass (and its subsequently Q-value) was recently measured at JYFL [51]. TRIUMF made its contribution by providing precise measurements on the branching ratio and the half-life of this isotope. Despite these high precision experiments, the uncertainty around the δ_C still dominates the total uncertainty of the F_t value at approximately 50%. Towner and Hardy approach using shell model with Saxon-Woods potential seems the most accepted approach. Due to a lack of experimental data, the value of the charge radius of ^{62}Ga included in their calculation of δ_C was extrapolated to be $\langle r_{ch}^2 \rangle = 3.94(10)$ fm. The extrapolation is based on electron scattering data on stable isotopes. From this extrapolation, $\delta_C = 1.47$. In terms of δ_{C1} and δ_{C2} gives $\delta_{C1} = 0.275(55)$ and $\delta_{C2} = 1.20(20)$, respectively. This thesis will provide the experimental validation of this approach, in light of other recent experimental results in the region.

Our series of measurements on neutron deficient gallium isotopes are an approach to an eventual measurement on ^{62}Ga .

References

- [1] B. Cheal, T. E. Cocolios, and S. Fritzsche. Laser spectroscopy of radioactive isotopes: Role and limitations of accurate isotope-shift calculations. *Phys. Rev. A*, 86:042501, Oct 2012.
- [2] C. Thibault, F. Touchard, S. Büttgenbach, et al. Hyperfine structure and isotope shift of the D_2 line of $^{76-98}\text{Rb}$ and some of their isomers. *Phys. Rev. C*, 23:2720–2729, Jun 1981.
- [3] M. Epherre, G. Audi, C. Thibault, et al. Direct measurements of the masses of rubidium and cesium isotopes far from stability. *Phys. Rev. C*, 19:1504–1522, Apr 1979.
- [4] J. C. Hardy and I. S. Towner. Superaligned $0^+ \rightarrow 0^+$ nuclear β decays: 2014 critical survey, with precise results for V_{ud} and CKM unitarity. *Phys. Rev. C*, 91:025501, Feb 2015.
- [5] C.J. Joachain B.H. Bransden. *Physics of Atoms and Molecules*. Longman Publishing, 1983.
- [6] Gordon W. F. Drake. *Handbook of Atomic Molecules and Optical Physics*. Springer, 2006.
- [7] H. Kopfermann. Nuclear moments, academic press, new york (1958) xiii-505 p. 95s. *nphysa*, 16:188–188, April 1960.
- [8] H. B. G. Casimir. *On the Interaction Between Atomic Nuclei and Electrons*. Freeman, (1963).
- [9] Klaus Blaum, Jens Dilling, and Wilfried Nörtershäuser. Precision atomic physics techniques for nuclear physics with radioactive beams. *Physica Scripta*, 2013(T152):014017, 2013.
- [10] Sune Svanberg. *Atomic Structure*, pages 4–28. Springer Berlin Heidelberg, Berlin, Heidelberg, 1991.

- [11] P. Aufmuth, K. Heilig, and A. Steudel. Changes in mean-square nuclear charge radii from optical isotope shifts. *Atomic Data and Nuclear Data Tables*, 37(3):455 – 490, 1987.
- [12] C. J. Foot. *Atomic Physics*. Oxford University Press, 2005.
- [13] J. Kantele. *Handbook of Nuclear Spectrometry*. Academic Press, 1995.
- [14] Jens Dilling, Reiner Krücken, and Lia Merminga. *ISAC and ARIEL: The TRIUMF Radioactive Beam Facilities and the Scientific Program*, volume 978-94-007-7962-4 (Print) 978-94-007-7963-1 (Online). Springer, 2014.
- [15] E. Mané, J. A. Behr, J. Billowes, et al. Collinear laser spectroscopy with reverse-extracted bunched beams at TRIUMF. *Hyperfine Interactions*, 199(1):357–363, 2011.
- [16] E. Mané, A. Voss, J. A. Behr, et al. First experimental determination of the charge radius of ^{74}Rb and its application in tests of the unitarity of the Cabibbo-Kobayashi-Maskawa matrix. *Phys. Rev. Lett.*, 107:212502, Nov 2011.
- [17] W. Z. Zhao, J. E. Simsarian, L. A. Orozco, and G. D. Sprouse. A computer-based digital feedback control of frequency drift of multiple lasers. *Review of Scientific Instruments*, 69(11):3737–3740, 1998.
- [18] Melles Griot. *Stabilized HeNe Laser System*, 1993.
- [19] Allen Leary. Collinear laser spectroscopy on neutron rich rubidium isotopes and development of a laser frequency locking system. Master’s thesis, McGill, 2014.
- [20] Eric D. Black. An introduction to Pound-Drever-Hall laser frequency stabilization. *American Journal of Physics*, 69(1):79–87, 2001.
- [21] A. Voss, F. Buchinger, B. Cheal, et al. Nuclear moments and charge radii of neutron-deficient francium isotopes and isomers. *Phys. Rev. C*, 91:044307, Apr 2015.
- [22] C. De Coster, K. Heyde, J.L. Wood, E.F. Zganjar. Electric monopole transitions from low energy excitations in nuclei. *Nuclear Physics A*, 651(4):323–368, 1999.
- [23] P. Möller, A.J. Sierk, R. Bengtsson, H. Sagawa, and T. Ichikawa. Global calculation of nuclear shape isomers. *Phys. Rev. Lett.*, 103:212501, Nov 2009.

- [24] P. Dabkiewicz, F. Buchinger, H. Fischer, et al. Nuclear shape isomerism in ^{185}Hg detected by laser spectroscopy. *Physics Letters B*, 82(2):199 – 203, 1979.
- [25] C. Thibault, F. Touchard, S. Büttgenbach, et al. Hyperfine structure and isotope shift of the D_2 line of $^{76-98}\text{Rb}$ and some of their isomers. *Phys. Rev. C*, 23:2720–2729, Jun 1981.
- [26] N.J. Stone. Table of nuclear magnetic dipole and electric quadrupole moments. *Atomic Data and Nuclear Data Tables*, 90(1):75 – 176, 2005.
- [27] Garnsworthy. Results from a run performed on the 8π spectrometer in december 2010.
- [28] V. Manea, D. Atanasov, D. Beck, et al. Collective degrees of freedom of neutron-rich $A \approx 100$ nuclei and the first mass measurement of the short-lived nuclide ^{100}Rb . *Phys. Rev. C*, 88:054322, Nov 2013.
- [29] V. V. Simon, T. Brunner, U. Chowdhury, et al. Penning-trap mass spectrometry of highly charged, neutron-rich Rb and Sr isotopes in the vicinity of $\mathbf{A} \approx 100$. *Phys. Rev. C*, 85:064308, Jun 2012.
- [30] Procter, T. J., Behr, J. A., Billowes, J., et al. Direct observation of an isomeric state in ^{98}Rb and nuclear properties of exotic rubidium isotopes measured by laser spectroscopy. *Eur. Phys. J. A*, 51(2):23, 2015.
- [31] P. Campbell, I. D. Moore, and M. R. Pearson. Laser spectroscopy for nuclear structure physics. *Progress in Particle and Nuclear Physics*, 86:127–180, 2016.
- [32] J Billowes and P Campbell. High-resolution laser spectroscopy for the study of nuclear sizes and shapes. *Journal of Physics G: Nuclear and Particle Physics*, 21(6):707, 1995.
- [33] Olivier T.J. Shelbaya. Laser spectroscopy of rare rubidium isotopes and development of data analysis software at TRIUMF. Master’s thesis, McGill University, 2012.
- [34] Balraj Singh. Nuclear data sheets for $a = 100$. *Nuclear Data Sheets*, 109(2):297 – 516, 2008.
- [35] G. Lhersonneau, B. Pfeiffer, R. Capote, et al. A $k = 3$ two-quasiparticle isomer in ^{98}Sr . *Phys. Rev. C*, 65:024318, Jan 2002.

- [36] G. Fricke and K. Heilig. Nuclear Charge Radii · ^{37}Rb Rubidium: Datasheet from Landolt-Börnstein - Group I Elementary Particles, Nuclei and Atoms · Volume 20: “Nuclear Charge Radii” in SpringerMaterials (http://dx.doi.org/10.1007/10856314_39). Copyright 2004 Springer-Verlag Berlin Heidelberg.
- [37] E. Browne and J.K. Tuli. Nuclear data sheets for $A = 99$. *Nuclear Data Sheets*, 112(2):275 – 446, 2011.
- [38] B. Cheal, J. Billowes, M. L. Bissell, et al. Discovery of a long-lived low-lying isomeric state in ^{80}Ga . *Phys. Rev. C*, 82:051302, Nov 2010.
- [39] T. J. Procter, J. Billowes, M. L. Bissell, et al. Nuclear mean-square charge radii of $^{63,64,66,68-82}\text{Ga}$ nuclei: No anomalous behavior at $N = 32$. *Phys. Rev. C*, 86:034329, Sep 2012.
- [40] Lépine-Szily, A., Lima, G. F., Villari, A. C. C., et al. Anomalous behaviour of matter radii of proton-rich Ga, Ge, As, Se and Br nuclei. *Eur. Phys. J. A*, 25:227–230, 2005.
- [41] K. S. Krane. *Introductory Nuclear Physics*. John Wiley and Sons, 1988.
- [42] S. Raman, C.W. Nestor Jr, and P. Tikkanen. Transition probability from the ground to the first excited 2^+ state of even-even nuclides. *Atomic Data and Nuclear Data Tables*, 78(1):1 – 128, 2001.
- [43] C. Corliss and W. Bozman. Experimental transition probabilities for spectral lines of seventy elements. *NBS Monograph*, 53, 1962.
- [44] J.H.M. Neijzen and A. Dönszelmann. Hyperfine structure and isotope shift measurements in neutral gallium and indium with a pulsed dye laser. *Physica B+C*, 98(3):235 – 241, 1980.
- [45] E. Kugler. The ISOLDE facility. *Hyperfine Interactions*, 23:129, 2000.
- [46] L.G. Mann, K.Glenn Tirsell, and S.D. Bloom. ^{64}Ga spin from $\beta - \gamma(\text{cp})$ correlation data and decay to ^{64}Zn levels. *Nuclear Physics A*, 97(2):425 – 443, 1967.
- [47] S. Fritzsche. Private communication.
- [48] M. Pearson. Hyperfine calculations for $Z=31$. Private communication.

- [49] I. Angeli and K.P. Marinova. Table of experimental nuclear ground state charge radii: An update. *Atomic Data and Nuclear Data Tables*, 99(1):69 – 95, 2013.
- [50] Yao W.-M. et al. Review of Particle Physics. *Journal of Physics G*, 33:1+, 2006.
- [51] T. Eronen, V. Elomaa, U. Hager, et al. Q-value of the superallowed β -decay of ^{62}Ga . *Physics Letters B*, 636(3–4):191 – 196, 2006.